Coordinated satellite, aircraft, and ground-based observations of a large transient methane release

Tai-Long He[1], Daniel J. Varon[1,2], Shobha Kondragunta[3], Xinrong Ren[4], Mark D. Cohen[4], Brian J. Carroll[5,6], Nathan Malarich[5,6], Jeffrey Peischl[5,7], Tobias A. de Jong[8], Jelmar Gerritsen[8], Joannes D. Maasakkers[8], Daniel H. Cusworth[9], Riley M. Duren[9], Steven S. Brown[6], Carsten Warneke[6], Colm Sweeney[7], Phillip Stratton[4,10], Alan Brewer[6], Sunil Baidar[5,6], Ezra J. T. Levin[11,12]

[1]Institute for Data, Systems, and Society, Massachusetts Institute of Technology, [2]Department of Aeronautics and Astronautics, Massachusetts Institute of Technology, [3]NOAA/NESDIS, [4]NOAA Air Resources Laboratory, [5]Cooperative Institute for Research in Environmental Sciences (CIRES), University of Colorado Boulder, [6]NOAA Chemical Sciences Laboratory, [7]NOAA Global Monitoring Laboratory, [8]SRON Space Research Organisation Netherlands, [9]Carbon Mapper, Inc, [10]Department of Atmospheric and Oceanic Science / Cooperative Institute for Satellite Earth System Studies (CISESS), University of Maryland, [11]Energy Institute, Colorado State University, [12]Department of Systems Engineering, Colorado State University.

*Tai-Long He, Daniel J. Varon.

Email: tlhe@mit.edu, dvaron@mit.edu

June 2026

==========

This is a non-peer-reviewed preprint submitted to EarthArXiv that is subject to change in subsequent versions. Please feel free to reach out to us if you have any questions or comments about the paper.

==========

Abstract

We present the results of a Very Large Methane Release (VLMR) experiment evaluating methane retrievals from the Geostationary Operational Environmental Satellites (GOES) Advanced Baseline Imagers (ABIs) and multiple low-Earth-orbit satellite instruments with high point-source detection thresholds. The experiment coordinated observations of a U.S. gas pipeline blowdown with nine satellites, an aircraft, and a truck-based mobile laboratory. We used the GOES-16, -18, and -19 ABIs with revisits every 10 min to 7 s to quantify release magnitude and associated uncertainty. Best methane retrieval precision of 7% was achieved in the 30-s mesoscale scan modes averaged to 5 min, yielding an estimated methane plume detection threshold of 15–30 t h^{-1} per m s^{-1} of wind. GOES detected total emissions of 370±30 t over 44–65 min from two release points. Source rate and mass estimates are broadly consistent across measurement platforms, but the total detected release mass is ~25% lower than that reported by the operator based on pipeline volume and pressure. This discrepancy may reflect late-stage emissions below satellite detection thresholds and indicates a potential low bias in satellite estimates of total emissions from large transient releases. Coordinated field experiments such as VLMR can complement existing controlled-release satellite evaluation programs by providing a framework to validate observations of very large methane point sources.

Significance Statement

Methane is a potent greenhouse gas, and emissions from oil and gas infrastructure are a major mitigation target. Satellites are increasingly used to detect and quantify these emissions, but evaluating their estimates of releases remains challenging. In this study, we analyze a U.S. gas pipeline blowdown in New Mexico using coordinated observations from nine satellites, two aircraft, and a truck-based mobile laboratory. Our experiment provides a rare opportunity to evaluate the accuracy of satellite-based observations of large, short-lived methane point sources. We show that geostationary satellites can continuously track and quantify such releases, with emission estimates consistent with other platforms and expectations from pipeline pressure and volume. Our results build confidence in satellite observations to monitor extreme methane releases worldwide.

Introduction

Methane is a potent greenhouse gas whose concentration is rapidly increasing in the atmosphere, posing a major challenge for climate change mitigation. A small number of high-emitting point sources account for a disproportionate fraction of total methane emissions (Duren et al., 2019; Lauvaux et al., 2022). Satellite observations have become an important tool for detecting and quantifying these sources to identify effective mitigation opportunities (Jacob et al., 2022). A growing constellation of low-Earth-orbit (LEO) satellite instruments provides a wide array of complementary capabilities for monitoring methane point sources, ranging from high-resolution imagers for targeted detection of relatively small plumes (0.1–1 t h^{-1}) to wide-swath instruments with lower sensitivity but greater spatial and temporal coverage enabling detection of large releases (>10 t h^{-1}) over broad areas (Jervis et al., 2021; Schuit et al., 2023; Duren et al., 2025). More recently, methane point-source monitoring has extended to geostationary orbit (GEO), enabling continuous hemispheric observations every few minutes and the detection of extreme, transient releases on the order of tens to hundreds of tonnes per hour (Watine-Guiu et al., 2023; Zhou et al., 2026).

Despite this progress, substantial uncertainties remain in satellite detection thresholds and quantification accuracy, particularly for high-emitting sources. Previous studies have evaluated detection and quantification performance indirectly, based on the population statistics of detected plumes (e.g., Lauvaux et al., 2022; Schuit et al., 2023; Ayasse et al., 2024) or analysis of synthetic plume data (e.g., Cusworth et al., 2019; Gorrono et al., 2023). Detection and quantification performance has also been directly evaluated using controlled release experiments with metered ground-truth source rates, which are increasingly common but have so far been limited to sources below 10 t h^{-1} due to cost and safety constraints (Sherwin et al., 2023, 2024;

Worden et al., 2025). These experiments provide valuable benchmarks for instruments with detection thresholds of ~1 t h^{-1} or lower, but are not well-suited to evaluating higher-threshold instruments (~10 t h-1 or larger) such as the Tropospheric Monitoring Instrument (TROPOMI) in LEO and the GOES Advanced Baseline Imager (ABI) in GEO.

Here we present the results of a Very Large Methane Release (VLMR) experiment evaluating the ability of such instruments to detect and quantify emissions. The experiment was conducted on 8 October 2024 in New Mexico, U.S., and involved coordinated observations of a planned gas pipeline blowdown with a suite of ground, aerial, and satellite platforms. We quantify the resulting emissions using observations from three GOES ABIs, six LEO instruments, an aircraft, and a truck-based mobile laboratory. The GOES ABI observations from three vantage points in GEO provide measurement frequencies of 10 min down to 7 s, allowing estimation of time-dependent plume mass, emission rate, and associated uncertainties. The LEO instruments provide additional snapshots of the evolving plumes, and the aircraft and ground-based platforms provide independent estimates of source rate along with detailed information on the timing of the blowdown, local meteorology, and in-situ methane concentrations. Estimates of total plume mass and source rate are compared across measurement platforms and benchmarked against the operator's reported release mass based on pipeline pressure and volume.

Experimental setup

Figure 1 illustrates the VLMR experimental setup. The blowdown occurred at two release points along the pipeline, hereafter referred to as the eastern and western sites. Emissions began at 17:23 UTC (LT+6) at the western site and 17:36 UTC at the eastern site. The pipeline operator reported total emissions of 27.5 million standard cubic feet (scf) of natural gas, corresponding to 506 t of methane at 96% methane content. The plumes were observed from space by the GOES-16, -18, and -19 ABIs; TROPOMI; the Visible Infrared Imaging Radiometer Suite (VIIRS) on the Suomi-NPP, NOAA-20, and NOAA-21 satellites; the PACE Ocean Color Instrument (OCI); and the Sentinel-3A Sea and Land Surface Temperature Radiometer (SLSTR). In situ measurements were from a Mooney aircraft equipped with a gas concentration analyzer and NOAA's Pick-Up Based Mobile Atmospheric Sounder (PUMAS) platform.

At the time of the VLMR experiment, GOES-16 and -18 were in their East and West positions at 75.2°W and 137.2°W, respectively, and GOES-19 was undergoing commissioning at 90°W. In addition to the operational 5–10-min scan modes from GOES-16 and -18, we scheduled 30-s targeted mesoscale scans with GOES-18, and the commissioning of GOES-19 provided an opportunity to test an experimental 7-s mesoscale scan mode. The mesoscale scans targeted a ~1000×1000-km^2 domain centered on the pipeline release points. In total, we analyze five continuous data streams from the three GOES satellites. The LEO satellites observed the releases primarily in the local afternoon (19:04–20:45 UTC), with one morning pass by Sentinel-

3A (17:35 UTC). More detailed information on the measurement platforms and scan modes is provided in the Materials and Methods section.

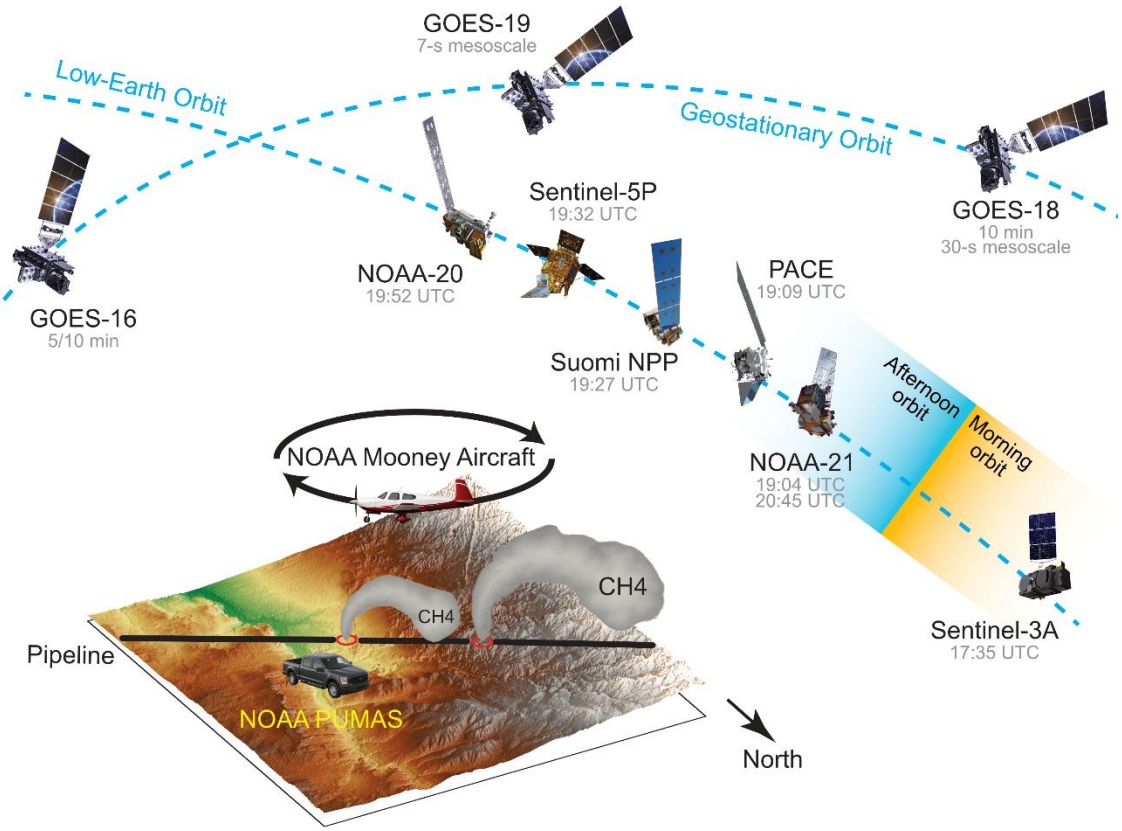

Figure 1. Schematic of the 8 October 2024 VLMR experiment to quantify methane (CH4) emissions from a planned gas pipeline blowdown in New Mexico, U.S. Measurements were collected from 3 GOES satellites, 6 LEO satellites, a Mooney aircraft, and a truck-based mobile laboratory. GOES scan frequencies (5/10-min operational modes and targeted 7–30-s mesoscale modes) and LEO overpass times (UTC; LT+6) are annotated in gray. The red circles indicate the two locations along the pipeline where the blowdown occurred.

Release mass estimates

Figure 2 presents snapshot retrievals of methane enhancements from the three GOES and six LEO satellites, together with observational (top-down) and modeled (bottom-up) estimates of plume mass over time. The plumes were first detected in the GOES mesoscale scans at 17:27 UTC and 17:38 UTC. Supplemental Movie S1 shows their full temporal evolution as observed from GEO. The eastern plume detached from its source at 18:20 UTC and the western plume at 18:30 UTC, corresponding to observed emission durations of 40–60 min, respectively (Fig. 2A, B). The LEO instruments captured the releases at a sequence of overpass times and show broad agreement with the GOES retrievals in plume magnitude, location, and extent (Fig. 2C, D), despite substantial differences in pixel size, viewing geometry, and retrieval precision. VIIRS, Sentinel-3 SLSTR, and PACE OCI, with nadir pixel resolutions of 500 m to 1 km, clearly resolve plume structure. Methane enhancements are strongly diluted within the coarser TROPOMI pixels (~5.5×7 km^2 at nadir), softening plume edges and broadening the apparent footprints. GOES ABI's high temporal

resolution and intermediate spatial resolution (~2 km at nadir) captures sufficient structural detail to track the spatiotemporal evolution of the plumes.

The observed plume mass, expressed in Figure 2E as integrated methane enhancement (IME; Frankenberg et al., 2016), exhibits an initial growth phase followed by stabilization as the plumes detach from their sources and are advected downwind, consistent with previous GEO satellite observations of large transient releases (Zhou et al., 2026). LEO satellites are limited to discrete overpass times, and in this case captured the release near the onset and after plume detachment but missed much of the growth phase. This illustrates a general limitation of LEO platforms for quantifying transient methane sources, whose episodic nature may prevent satellites with fixed overpass times from detecting actual release locations or observing specific stages of plume development. GOES ABI infers a total detectable methane mass of 370 ± 30 t, with 260 ± 40 t from the western source and 100 ± 50 t from the eastern source, while LEO estimates for total mass range from 310 ± 100 t to 420 ± 65 t (individual source breakdown shown in Fig. S13), generally within 5–15% of the GOES multi-instrument mean and consistent within uncertainties.

The pipeline operator's reported total release of 506 t is considerably higher than satellite IME estimates: 27% higher than our GOES estimate, and 17–39% higher than our estimates from the LEO instruments, with the most precise retrieval from PACE OCI (see Text S5) yielding the smallest mass bias. The dashed line in Figure 2E models the blowdown releases as two exponential decay processes (see Materials and Methods), with a total duration of 3 hours for the pipeline to reach atmospheric pressure, as reported by the operators. This bottom-up estimate agrees closely with the IME inferred from GOES ABI and Sentinel-3 SLSTR during the plume growth phase (~17:22–18:00 UTC), but diverges during the stabilization phase, when the satellite-observed mass begins to fall below the modeled trajectory. This discrepancy may reflect the satellites' failure to capture emissions below their detection thresholds, which occur later in the release. It may also reflect weak, dispersed enhancements that were not captured by the plume masks. While the satellites effectively track the initial methane pulses over the first hour of the

blowdown, the detected mass should be interpreted as a lower bound on total emissions. In this case, it underestimates the total by about 25%.

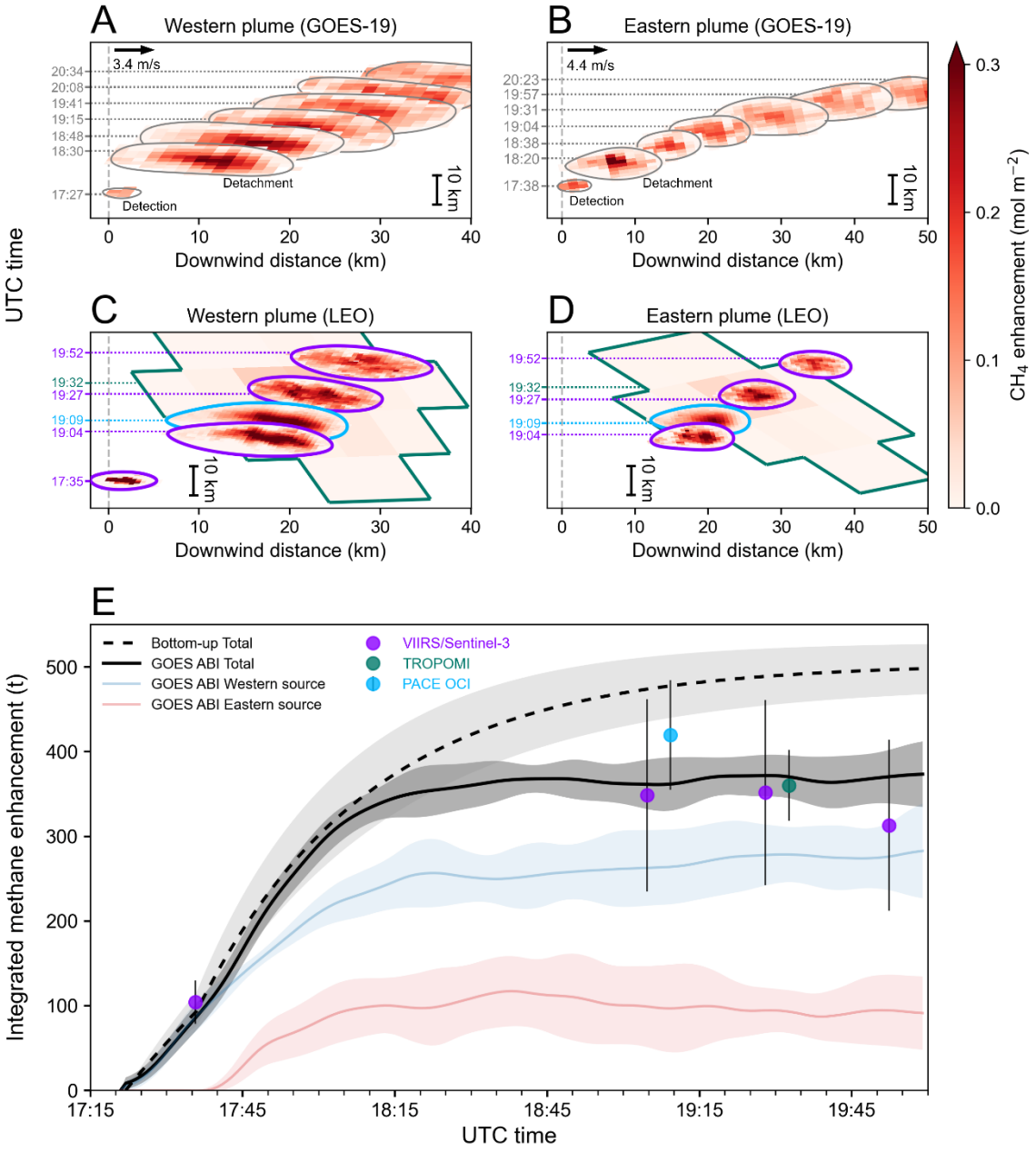

Figure 2. Methane plume evolution observed by GEO and LEO satellites during the pipeline blowdown. (A,B) Sequential GOES-19 ABI retrievals showing masked methane enhancements downwind of the two sources, with plume mask contours (smoothed for visualization) in grey. Plumes are vertically offset in time to reduce overlap for visualization. First detection and detachment snapshots are labeled. Local wind speed estimates from the High-Resolution Rapid Refresh (HRRR) product are shown inset. (C,D) Same as (A,B) but for LEO satellite observations at different overpass times. Plume contour lines and overpass times are color-coded by instrument consistently with the markers in panel (E). The latest NOAA-21 pass, at 20:45 UTC (Fig. S2), is not shown. (E) Time series of total methane plume mass, expressed as integrated methane

enhancement (IME). Solid lines show the mean IME across the five GOES ABI scan modes interpolated to 1 min and smoothed with a 9-min moving average (Materials and Methods). The blue and red lines are for the western and eastern sources, respectively, and the black line is for their sum. Dark grey shading indicates ±1σ uncertainty ranges derived from the five GOES ABI scan modes. The circular markers represent IME derived from LEO satellites for the sum of both plumes. The dashed line shows bottom-up estimates based on pipeline pressure and volume reported by the operators, modeling the release as an exponential decay process. Light grey shading shows the propagated uncertainty in the bottom-up estimates from the release duration and total release mass (Materials and Methods).

Source rate estimates

Quantifying source rates from single-pass plume images typically requires information on the local wind speed, which is highly uncertain (Varon et al., 2018). Here the fine sampling frequency of GOES ABI enables a wind-free source-rate retrieval based on temporal changes in plume mass, which capture variability in emissions that single-pass retrievals cannot easily resolve (Watine-Guiu et al., 2023). Figure 3 shows instantaneous source rates inferred from ABI retrievals as the time derivative of IME for each plume from initial release to detachment. We find that the source rate peaked at about 500 t h^{-1} for the western source and 360 t h^{-1} for the eastern source within 10 minutes of the onset of the releases, and then declined over the following ~30–60 min. The initial growth in source rate (dotted lines in Fig. 3) likely reflects nonlinear absorption effects from strong sub-pixel concentration gradients early in the release. Increasing the methane concentration within a dense sub-pixel plume would produce only small changes in the pixel-average radiance, biasing retrievals low. This effect would weaken as the plume diffuses across one or more full pixels.

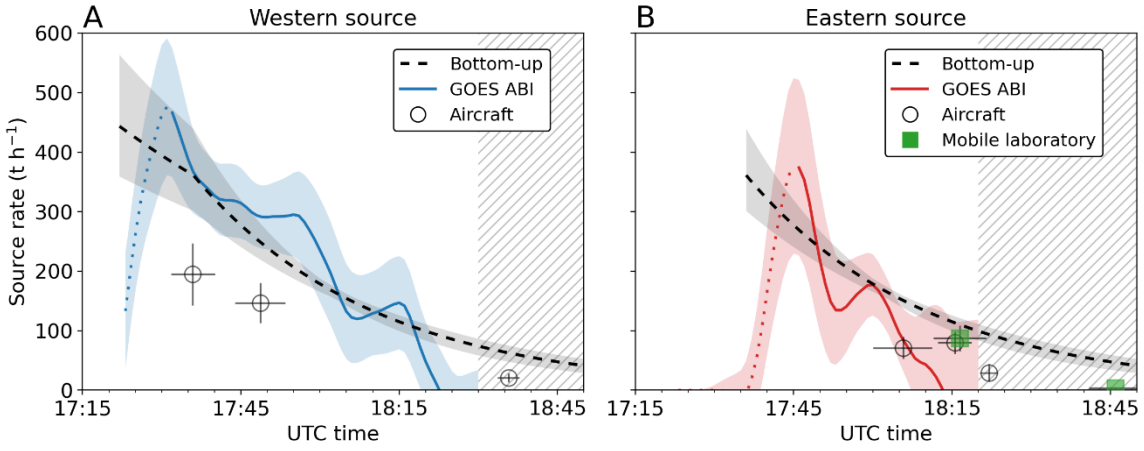

Figure 3. Instantaneous source rates for the (A) western and (B) eastern sources inferred from GOES ABI and in situ measurements. ABI source rates are defined as the time derivative of IME (Fig. 2). Dotted line segments mark periods of initial mass accumulation when instantaneous fluxes are not well defined (see text). Solid lines show the mean source rate across the five GOES ABI retrievals, blue/red shaded regions indicate ±1σ uncertainties, and the hatched regions mark the period after plume detachments. Dashed lines represent bottom-up estimates based on total release mass (~500 t methane) and blowdown duration (3 h) as reported by the pipeline operators. Light grey shading shows uncertainty in the bottom-up estimates from release duration and total release mass (Materials and Methods). Circular and square markers show source-rate estimates derived from in situ measurements using aircraft and ground-based mass-balance calculations.

Our GOES ABI-derived source rates agree with the bottom-up exponential model within uncertainties for both release points. They show higher peak values and lower minima, dropping below zero as the emission signals approach the noise level of the retrieval shortly before plume detachment. Agreement between satellite-derived and in situ estimates is also within uncertainties

for the eastern source. For the western source, however, satellite-derived and bottom-up source-rate estimates are roughly a factor of two higher than inferred from the first two aircraft spirals. In situ estimates are generally lower than expected from the bottom-up model, with low biases of 40–70% for the western source and 20–90% for the eastern source.

We tested whether this low bias could reflect saturation of the Picarro analyzer outside its nominal operating range (0–20 ppm; Picarro, 2021) for the western source. The peak measured concentration during the VLMR experiment was 226 ppm, far outside the nominal range, but laboratory tests using a 193 ppm methane standard indicate that the instrument remains accurate at these elevated concentrations (Fig. S11). The bias is therefore more likely attributable to undersampling of the transient plume, which is not expected to be well-mixed within the boundary layer (Fig. S12). Future VLMR experiments could employ flight patterns with larger spiral radii to sample a more fully mixed plume, or multiple aircraft at different radii to better characterize plume evolution over the course of the release. The comparatively close agreement between GOES ABI and the bottom-up model highlights the value of geostationary satellite observations for quantifying methane plume mass and instantaneous source rate.

The limitations of the bottom-up model must also be recognized. It assumes equal partitioning of the release between the eastern and western sites, neglecting potential differences in vent geometry and supercritical fluid dynamics within the pipeline (Harris et al., 2025). It may also overestimate late-stage source rates by neglecting cooling during blowdown, including Joule-Thomson effects that can lead to icing or hydrate formation at the vent orifice, reducing the effective mass flow (API, 2020). Future VLMR experiments could incorporate on-site measurements of pressure and temperature along the pipeline, especially near the release points, to provide better ground-truth information on source rates over time.

Retrieval precision and detection threshold

The VLMR experiment provided an opportunity to characterize GOES ABI methane retrieval precision in different scan modes. Quantifying precision as the standard deviation of retrieved methane enhancements across scans and excluding pixels containing clouds, water, and plumes, we find best retrieval precision of 0.044 mol m^{-2} (7% of 1930 ppb background) in the 30-s scan mode averaged to 5 min, followed by 0.052 mol m^{-2} (8% of background) in the 7-s scan mode averaged to 5 min. Precision for the other ABI scan modes is 10%–12%. Sensitivity tests using different averaging windows show that 5-min averaging provides the best balance between noise reduction and plume signal preservation for both the 7-s and 30-s scans (Fig. S14, S15). Time-averaged mesoscale scans therefore provide a higher-precision complement to hemispheric scan modes for geostationary methane plume monitoring.

Finally, we use GOES ABI's fine temporal sampling to assess the plume detection threshold Q_{min} [t h^{-1}] for the VLMR scene. In the finest-precision 30-s mesoscale scan mode, the plumes are first detected at the single-pixel level with column enhancements of 0.07–0.08 mol m^{-2} over 3.35-km pixels, reflecting a single-pixel methane mass of ~12 t for initial detection. The steady-state emission rate required to sustain such an enhancement against horizontal transport across the pixel is Qmin = 15 t h^{-1} per m s^{-1} of wind, which we take as a lower bound on GOES ABI's detection threshold. We also estimate Q_{min} using the heuristic equation introduced by Jacob et al. (2016):

$$Q\_min = M_{CH_4} \cdot U \cdot L \cdot q \cdot \sigma \quad \text{(Eq. 1)}$$

where M_{CH_4} is the molar mass of methane, U [km h^{-1}] is the wind speed, pixel size L=3.35 km, and q is the number of standard deviations above the background noise level σ required for single-pixel detection (q=2 by convention). Under 4 m s^{-1} winds (Fig. 2) and assuming 7% precision for σ, this yields a minimum detectable source rate of 110 t h^{-1} (27 t h^{-1} per m s^{-1}), consistent with the uncertainty ranges in Fig. 3. We therefore estimate a detection threshold of 15–30 t h^{-1} per m s^{-1} of wind for GOES ABI for the VLMR scene. This is similar to the detection threshold of 30–50 t h^{-1}

estimated by Zhou et al. (2026) for the higher-resolution Meteosat Flexible Combined Imager (FCI) geostationary satellite instrument under 3–4 m s^{-1} winds (~10–15 t h^{-1} per m s^{-1} of wind).

Conclusions

We used a Very Large Methane Release (VLMR) experiment to evaluate satellite capabilities for quantifying large transient methane emissions through coordinated multi-platform observations of a planned U.S. gas pipeline blowdown. Continuous GOES ABI measurements from three instruments in five scan modes captured the evolution of the release with down to sub-minute temporal resolution and detected total methane emissions of 370 ± 30 t from two release points. The blowdown was also observed by six LEO satellite instruments, a Mooney aircraft, and a truck-based mobile laboratory. Estimates of total release mass are consistent across satellite platforms but ~25% lower than the operator's reported value based on pipeline pressure and volume. The satellite observations effectively track the initial methane pulses downwind but may miss weaker emissions below instrument detection thresholds later in the release. In situ mass-balance analysis underestimates early source rates by ~50%, reflecting the difficulty of sampling rapidly evolving, heterogeneous plumes from transient point sources. Our results confirm the capability of satellite instruments to quantify large transient methane releases from both low-Earth and geostationary orbit, while also revealing a potential low bias in total detected emissions. Expanding VLMR experiments across a broader range of observing conditions would further refine satellite performance characterization and improve understanding of the contribution of large transient releases to regional and global methane budgets.

Materials and Methods

GOES ABI GEO satellite data. GOES ABI is a multispectral scanning radiometer with 16 channels in the visible (VIS), near-infrared (NIR), and infrared (IR) that support a wide range of weather, ocean, and environmental monitoring applications. Pixel resolution is 0.5 km (VIS), 1 km (NIR), or 2 km (IR) at equatorial nadir. ABI has three operational scan modes that provide coverage of the full hemispheric disk every 10 minutes, the contiguous US (CONUS) every 5 minutes, and targeted mesoscale sectors (~1000×1000-km^2 domain) every 30–60 seconds. GOES-16 operated as GOES-East at 75.2°W from 2016 to 2025, covering the eastern US, Atlantic Ocean, and part of western Africa. It was superseded by GOES-19 in April 2025 and now serves as backup satellite at 104.7°W. GOES-18 currently serves as GOES-West at 137.2°W and covers the western US, Pacific Ocean, and Alaska.

We use the Level-1b (L1b) radiances and Level-2 (L2) cloud mask data from a total of five scan modes across all three ABIs to perform methane retrievals for the VLMR pipeline releases with sampling frequencies from 10 min down to 7 s.

GOES ABI can detect large transient methane releases in its shortwave-infrared (SWIR) bands at 1.6 μm and 2.25 μm via multi-band–multi-pass (MBMP) methane retrievals (Watine-Guiu et al., 2023). The retrievals compare images from the methane-sensitive 2.25-μm band with reference images from the 1.6-μm band and previous scans. To retrieve methane column concentrations, we define for each image pixel a band ratio

$$r = \frac{c * R_{2.25}}{R_{1.6}} \quad \text{(Eq. 2)}$$

where $R_{1.6}$ and $R_{2.25}$ represent the measured radiances in the 1.6-μm and 2.25-μm bands and c is a scaling factor to address differences in scene-wide mean brightness between the two bands. r is converted to methane column enhancement (mol m^{-2}) using a lookup-table derived from radiative transfer calculations. For each resulting retrieval image, we construct a plume-free reference retrieval image from previous (pre-blowdown) scans and subtract it to better isolate methane plumes from surface artifacts (see Text S2 for additional details).

To account for differences in observational scan times, each of the five GOES ABI data streams was first interpolated to a 1-min temporal resolution and then smoothed using a 9-min moving average. The IME values and source rates plotted in Figures 2 and 3 were computed as

the mean across the five streams, with error bars representing the standard deviation. Sensitivity tests using different averaging windows (5–15 min) show that the results are robust to this choice (Fig. S13).

LEO satellite data

TROPOMI. The TROPOspheric Monitoring Instrument (TROPOMI) is a high-spectral-resolution spectrometer on the Sentinel-5P satellite (Veefkind et al., 2012). Its local overpass time is around 13:30 local time (LT) and its methane retrieval product has a nadir pixel resolution of 5.5×7 km^2. TROPOMI's fine 0.25-nm spectral resolution enables high-quality methane retrievals with <1% precision (Lorente et al., 2022) and detection of large methane point sources (Schuit et al., 2023). We use the operational TROPOMI L2 total methane column data product (Copernicus Sentinel-5P, 2021) to quantify the total methane mass released during the VLMR experiment (Text S3). TROPOMI's fine retrieval precision makes it an effective baseline for evaluating methane plume mass estimates from less sensitive multispectral retrievals.

VIIRS and SLSTR. De Jong et al. (2025) demonstrated the use of multiple multispectral satellite radiometers for sub-daily monitoring of methane point sources, including VIIRS on the Suomi-NPP, NOAA-20, and NOAA-21 satellites, and SLSTR on the Sentinel-3A and -3B satellites (Pandey et al., 2023). The three VIIRS instruments fly in sun-synchronous afternoon orbits with observations around 13:30 LT, while the SLSTR instruments observe in the morning around 10:00 LT. The methane retrieval algorithm for VIIRS and SLSTR uses the difference of the ratios of reflectance between target and reference images in the 1.6- and 2.25-μm SWIR bands (see Text S4). The nadir spatial resolution of the methane retrieval is 750 m for VIIRS and 500 m for SLSTR. At these resolutions, facility-level methane plumes can be detected, and the sub-daily monitoring frequency combining all instruments makes it possible to capture short-lived emission events such as pipeline blowdowns.

OCI. The Ocean Color Instrument (OCI) is an imaging radiometer on NASA's Plankton, Aerosol, Cloud, ocean Ecosystem (PACE) satellite, launched in February 2024. OCI provides SWIR measurements at 1.6, 2.1, and 2.3 μm with 1.2-km spatial resolution. The 2.1-μm band exhibits weak methane absorption and is spectrally closer than the 1.6-μm band to the methane-sensitive 2.3-μm band, making it a more effective methane-free reference channel for MBMP retrievals. Details about the OCI methane retrieval algorithm are given in Text S5.

Aircraft data NOAA Global Monitoring Laboratory performed ~1 km radius spiral profiles around the two release sites and flew cross-plume transects ~25 km downwind of the western site (Fig. S5) using a ChampionX Mooney aircraft instrumented with a Picarro 2401-m gas concentration analyzer. Methane mixing ratios were measured every 2.5 seconds and interpolated to 1 Hz, with estimated uncertainties of ±2 ppb. We use these measurements to estimate emission rates Q [kg h^{-1}] for both pipeline release points using a mass-balance approach:

$$Q = \int \left[\frac{M_{CH_4}}{M_{air}} \cdot \rho_{air} \cdot 10^{-9}\right] \cdot [C(t) - C_b] \cdot U_p(t) \cdot dA \quad \text{(Eq.3)}$$

Here C(t) is the measured methane concentration, C_b is the background concentration, $U_p(t)$ is the wind velocity component perpendicular to the plume cross-section, dA is a differential element of the plume cross-sectional area with vertical extent defined by the helix pitch for spirals (Conley et al., 2017) or the boundary layer height for cross-plume transects (Peischl et al., 2015). The factor $\frac{M_{CH_4}}{M_{air}} \cdot \rho_{air} \cdot 10^{-9}$ converts methane mixing ratios from nmol mol^{-1} to mass concentration, where M_{CH4} and M_{air} are the molecular weights of methane and dry air, respectively, and ρ_{air} is the air density (see Text S6). Wind speed and direction used in the mass-balance calculations and shown in Figure 2 are taken from the hourly High-Resolution Rapid Refresh (HRRR; Dowell et al., 2022) reanalysis at 10 m above ground level.

NASA's Airborne Visible/Infrared Imaging Spectrometer-3 (AVIRIS-3), a high-spectral-resolution imager supporting methane point-source detection at 4.2 m spatial resolution, was also operating in the region at the time of the experiment. It was diverted from a nearby research flight

track and captured methane enhancements from a test release at 16:13 UTC prior to blowdown at the eastern release site (Fig. S5).

Ground-based measurements. NOAA Chemical Sciences Laboratory performed ground-based measurements with the Pick-Up Based Mobile Atmospheric Sounder (PUMAS) platform to estimate emission rates from plume transects downwind of the eastern source. PUMAS is a motion-stabilized Doppler lidar (Carroll et al., 2025), augmented for this experiment with an Aeris mid-infrared absorption analyzer measuring methane and ethane at 1 Hz.

We calculate the mass flux for 10-min transects across the eastern plume ~9 km downwind of the source location using the mass-balance approach of Eq. 3, assuming the plume is vertically well-mixed in one vertical layer with cross-sectional area dA. The equation variables are derived from PUMAS measurements of methane mixing ratio, mixed-layer height, and 3D lidar wind fields. The calculated mass flux is assigned to an earlier pipeline release time based on estimated transport time between pipeline and transect (see Text S7).

Bottom-up exponential decay model

We model the methane release from the pipeline as an exponential decay process describing the depressurization of the pipeline from initial to atmospheric pressure. Based on the operator's reported total gas release of 27.5 million scf (506 t methane) and release duration of 3 h, the cumulative release methane mass at each site (MW and ME) is modeled across two emission stages as follows:

$$M_W(t) = \begin{cases} M_{W,0}\left(1 - e^{-\frac{t-t_0}{\tau_1}}\right), t_0 \le t < t_E \\ M_W(t_E) + M'_{W,0}\left(1 - e^{-\frac{t-t_E}{\tau_2}}\right), t \ge t_E \end{cases}$$

$$M_E(t) = \begin{cases} 0, t < t_E \\ M_{E,0}\left(1 - e^{-\frac{t-t_E}{\tau_2}}\right), t \ge t_E \end{cases}$$

where t_0 and t_E are the onset times of the western and eastern releases, respectively, $M_{W,0}$ = 506 t and $M_{W,0}$' are the asymptotic release masses of the western source in each stage, $M_{E,0} = M_{W,0}$' is the asymptotic release mass of the eastern source, and τ_1 and τ_2 are the decay time constants before and after the eastern valve opened. The reported total release duration of 3 h implies τ_1= 60 min and τ_2= 30 min. Fitting the decay model to the GOES ABI IME data yields similar values of τ_1= 62 min and τ_2= 31 min, implying a total duration of 186 min to achieve atmospheric pressure.

The uncertainty associated with the bottom-up estimates in Figures 2 and 3 is estimated by combining a ±5% uncertainty in the operator-reported total release mass with release durations of 150, 180, and 210 min (spanning 5τ to 7τ). The shaded envelope spans the range across all combinations of the upper and lower bounds of these two parameters.

Data, Materials, and Software Availability

The NOAA GOES Level-1b radiances and Level-2 cloud mask products are publicly available via the AWS Open Data Registry (https://registry.opendata.aws/noaa-goes). The GOES ABI retrieved methane total columns have been deposited in Zenodo (https://doi.org/10.5281/zenodo.18443915) (He et al., 2026). TROPOMI Level-2 methane retrievals and Sentinel-3 Level-1 radiances are available from the Copernicus data services (https://www.copernicus.eu). VIIRS and PACE-OCI Level-1 radiances are available from NASA Earthdata (https://earthdata.nasa.gov).

Acknowledgments

We thank Pipeline Research Council International (PRCI) for their assistance coordinating the experiment. The project was supported by NOAA NESDIS (Contract #1332KP24C0023). The views expressed are those of the authors and do not necessarily reflect any position of NOAA or

the Department of Commerce. T.A.d J. acknowledges funding from the IMEO Science Studies programme contract DTIE22-EN5036. Part of the work by J.G. was done in the scope of his M.Sc. program at Delft University of Technology. We thank Daniel T. Lindsey for his support in planning the GOES-19 7-second targeted observations.

References

1. Duren, R.M., Thorpe, A.K., Foster, K.T. et al. California's methane super-emitters. Nature 575, 180–184 (2019). https://doi.org/10.1038/s41586-019-1720-3
2. Lauvaux et al. ,Global assessment of oil and gas methane ultra-emitters. Science375,557-561(2022).DOI:10.1126/science.abj4351
3. Jacob, D. J., Varon, D. J., Cusworth, D. H., Dennison, P. E., Frankenberg, C., Gautam, R., Guanter, L., Kelley, J., McKeever, J., Ott, L. E., Poulter, B., Qu, Z., Thorpe, A. K., Worden, J. R., and Duren, R. M.: Quantifying methane emissions from the global scale down to point sources using satellite observations of atmospheric methane, Atmos. Chem. Phys., 22, 9617–9646, https://doi.org/10.5194/acp-22-9617-2022, 2022.
4. Jervis, D., McKeever, J., Durak, B. O. A., Sloan, J. J., Gains, D., Varon, D. J., Ramier, A., Strupler, M., and Tarrant, E.: The GHGSat-D imaging spectrometer, Atmos. Meas. Tech., 14, 2127–2140, https://doi.org/10.5194/amt-14-2127-2021, 2021.
5. Schuit, B. J., Maasakkers, J. D., Bijl, P., Mahapatra, G., van den Berg, A.-W., Pandey, S., Lorente, A., Borsdorff, T., Houweling, S., Varon, D. J., McKeever, J., Jervis, D., Girard, M., Irakulis-Loitxate, I., Gorroño, J., Guanter, L., Cusworth, D. H., and Aben, I.: Automated detection and monitoring of methane super-emitters using satellite data, Atmos. Chem. Phys., 23, 9071–9098, https://doi.org/10.5194/acp-23-9071-2023, 2023.
6. Duren, R., Cusworth, D., Ayasse, A., Howell, K., Diamond, A., Scarpelli, T., Kim, J., O'neill, K., Lai-Norling, J., Thorpe, A., Zandbergen, S. R., Shaw, L., Keremedjiev, M., Guido, J., Giuliano, P., Goldstein, M., Nallapu, R., Barentsen, G., Thompson, D. R., Roth, K., Jensen, D., Eastwood, M., Reuland, F., Adams, T., Brandt, A., Kort, E. A., Mason, J., and Green, R. O.: The Carbon Mapper emissions monitoring system, Atmos. Meas. Tech., 18, 6933–6958, https://doi.org/10.5194/amt-18-6933-2025, 2025.
7. Watine-Guiu, D.J. Varon, I. Irakulis-Loitxate, N. Balasus, & D.J. Jacob, Geostationary satellite observations of extreme and transient methane emissions from oil and gas infrastructure, Proc. Natl. Acad. Sci. U.S.A. 120 (52) e2310797120, https://doi.org/10.1073/pnas.2310797120 (2023).
8. Zhou, S., Gorroño, J., Roger, J., Irakulis-Loitxate, I., Lindstrot, R., Pei, Z., Si, L., and Guanter, L.: Assessing the Potential of the MTG-FCI Geostationary Mission for the Detection of Methane Plumes, Environ. Sci. Technol., 60, 6137–6148, https://doi.org/10.1021/acs.est.5c07974, 2026.
9. Ayasse, A. K., Cusworth, D. H., Howell, K., O'Neill, K., Conrad, B. M., Johnson, M. R., Heckler, J., Asner, G. P., & Duren, R. (2024). Probability of detection and multi-sensor persistence of methane emissions from coincident airborne and satellite observations. Environmental Science & Technology, 58(49), 21536–21544.
10. Cusworth, D. H., Jacob, D. J., Varon, D. J., Chan Miller, C., Liu, X., Chance, K., Thorpe, A. K., Duren, R. M., Miller, C. E., Thompson, D. R., Frankenberg, C., Guanter, L., and Randles, C. A.: Potential of next-generation imaging spectrometers to detect and quantify methane point sources from space, Atmos. Meas. Tech., 12, 5655–5668, https://doi.org/10.5194/amt-12-5655-2019, 2019.
11. Gorroño, J., Varon, D. J., Irakulis-Loitxate, I., and Guanter, L.: Understanding the potential of Sentinel-2 for monitoring methane point emissions, Atmos. Meas. Tech., 16, 89–107, https://doi.org/10.5194/amt-16-89-2023, 2023.
12. Sherwin, E.D., Rutherford, J.S., Chen, Y. et al. Single-blind validation of space-based point-source detection and quantification of onshore methane emissions. Sci Rep 13, 3836 (2023). https://doi.org/10.1038/s41598-023-30761-2

13. Sherwin, E. D., El Abbadi, S. H., Burdeau, P. M., Zhang, Z., Chen, Z., Rutherford, J. S., Chen, Y., and Brandt, A. R.: Single-blind test of nine methane-sensing satellite systems from three continents, Atmos. Meas. Tech., 17, 765–782, https://doi.org/10.5194/amt-17-765-2024, 2024.
14. Worden, J., Green, P., Eldering, A., & Sherwin, E. (2025). Common practices for quantifying methane emissions from plumes detected by remote sensing (NIST Interagency/Internal Report NIST.IR.8575). National Institute of Standards and Technology. https://doi.org/10.6028/NIST.IR.8575
15. C. Frankenberg,A.K. Thorpe,D.R. Thompson,G. Hulley,E.A. Kort,N. Vance,J. Borchardt,T. Krings,K. Gerilowski,C. Sweeney,S. Conley,B.D. Bue,A.D. Aubrey,S. Hook, & R.O. Green, Airborne methane remote measurements reveal heavy-tail flux distribution in Four Corners region, Proc. Natl. Acad. Sci. U.S.A. 113 (35) 9734-9739, https://doi.org/10.1073/pnas.1605617113 (2016).
16. Varon, D. J., Jacob, D. J., McKeever, J., Jervis, D., Durak, B. O. A., Xia, Y., and Huang, Y.: Quantifying methane point sources from fine-scale satellite observations of atmospheric methane plumes, Atmos. Meas. Tech., 11, 5673–5686, https://doi.org/10.5194/amt-11-5673-2018, 2018.
17. Picarro, Inc. (2021). G2401 CO2/CO/CH4/H2O Concentration Analyzer Datasheet. Santa Clara, CA. Available at https://www.picarro.com/sites/default/files/product_documents/Picarro_G2401%20Datasheet_211029.pdf
18. Harris, S.J., Schwietzke, S., France, J.L. et al. Methane emissions from the Nord Stream subsea pipeline leaks. Nature 637, 1124–1130 (2025). https://doi.org/10.1038/s41586-024-08396-8.
19. American Petroleum Institute. (2020). Pressure-relieving and depressuring systems (SEVENTH). https://dl.eiepd.com/libraries/product/operation-to-design/From-Operation-to-Design-References-Software/API/API%20521-Jun%202020_7th%20Edition-EIEPD%20Package%20Marked.pdf
20. Jacob, D. J., Turner, A. J., Maasakkers, J. D., Sheng, J., Sun, K., Liu, X., Chance, K., Aben, I., McKeever, J., and Frankenberg, C.: Satellite observations of atmospheric methane and their value for quantifying methane emissions, Atmos. Chem. Phys., 16, 14371–14396, https://doi.org/10.5194/acp-16-14371-2016, 2016.
21. J.P. Veefkind, I. Aben, K. McMullan, H. Förster, J. de Vries, G. Otter, J. Claas, H.J. Eskes, J.F. de Haan, Q. Kleipool, M. van Weele, O. Hasekamp, R. Hoogeveen, J. Landgraf, R. Snel, P. Tol, P. Ingmann, R. Voors, B. Kruizinga, R. Vink, H. Visser, P.F. Levelt, TROPOMI on the ESA Sentinel-5 Precursor: A GMES mission for global observations of the atmospheric composition for climate, air quality and ozone layer applications, Remote Sensing of Environment, Volume 120, 2012, Pages 70-83, ISSN 0034-4257, https://doi.org/10.1016/j.rse.2011.09.027.
22. Lorente, A., Borsdorff, T., Martinez-Velarte, M. C., Butz, A., Hasekamp, O. P., Wu, L., and Landgraf, J.: Evaluation of the methane full-physics retrieval applied to TROPOMI ocean sun glint measurements, Atmos. Meas. Tech., 15, 6585–6603, https://doi.org/10.5194/amt-15-6585-2022, 2022.
23. Copernicus Sentinel ‐ 5P. (2021). TROPOMI level 2 methane total column [dataset]. European Space Agency. doi: 10.5270/s5p-3lcdqiv.
24. de Jong, T. A., Maasakkers, J. D., Irakulis-Loitxate, I., Randles, C. A., Tol, P., & Aben, I. (2025). Daily global methane super-emitter detection and source identification with sub-daily tracking. Geophysical Research Letters, 52, e2024GL111824. https://doi.org/10.1029/2024GL111824
25. Sudhanshu Pandey, Maarten van Nistelrooij, Joannes D. Maasakkers, Pratik Sutar, Sander Houweling, Daniel J. Varon, Paul Tol, David Gains, John Worden, Ilse Aben, Daily detection and quantification of methane leaks using Sentinel-3: a tiered satellite observation approach with Sentinel-2 and Sentinel-5p, Remote Sensing of Environment, Volume 296, 2023, 113716, ISSN 0034-4257, https://doi.org/10.1016/j.rse.2023.113716.

26. Conley, S., Faloona, I., Mehrotra, S., Suard, M., Lenschow, D. H., Sweeney, C., Herndon, S., Schwietzke, S., Pétron, G., Pifer, J., Kort, E. A., and Schnell, R.: Application of Gauss's theorem to quantify localized surface emissions from airborne measurements of wind and trace gases, Atmos. Meas. Tech., 10, 3345–3358, https://doi.org/10.5194/amt-10-3345-2017, 2017.
27. Peischl, J., Ryerson, T. B., Aikin, K. C., deGouw, J. A., Gilman, J. B., Holloway, J. S., Lerner, B. M., Nadkarni, R., Neuman, J. A., Nowak, J. B., Trainer, M., Warneke, C. and Parrish, D. D. (2015), Quantifying atmospheric methane emissions from the Haynesville, Fayetteville, and northeastern Marcellus shale gas production regions. J. Geophys. Res. Atmos., 120: 2119–2139. doi: 10.1002/2014JD022697.
28. Dowell, D. C., and Coauthors, 2022: The High-Resolution Rapid Refresh (HRRR): An Hourly Updating Convection-Allowing Forecast Model. Part I: Motivation and System Description. Wea. Forecasting, 37, 1371–1395, https://doi.org/10.1175/WAF-D-21-0151.1.
29. Carroll, B. J., Strobach, E., Baidar, S., Holloway, M. W., McCarty, B., Marchbanks, R., & Brewer, W. A. (2025). Wildfire smoke shading observations: Impacts on boundary layer mixing and thermally driven smoke transport. Journal of Geophysical Research: Atmospheres, 130, e2024JD043303. https://doi.org/10.1029/2024JD043303
30. He, T.-L., Varon, D., Kondragunta, S., Ren, X., Cohen, M., Carroll, B., Malarich, N., Peischl, J., de Jong, T., Gerritsen, J., Maasakkers, J., Cusworth, D., Duren, R., Brown, S., Warneke, C., Sweeney, C., Stratton, P., Brewer, A., Baidar, S., & Levin, E. (2026). Replication Data for: Coordinated satellite, aircraft, and ground-based observations of a large transient methane release [Data set]. Zenodo. https://doi.org/10.5281/zenodo.18443915

Supporting Information for

Coordinated satellite, aircraft, and ground-based observations of a large transient methane release.

Tai-Long He[1], Daniel J. Varon[1,2], Shobha Kondragunta[3], Xinrong Ren[4], Mark D. Cohen[4], Brian J. Carroll[5,6], Nathan Malarich[5,6], Jeffrey Peischl[5,7], Tobias A. de Jong[8], Jelmar Gerritsen[8], Joannes D. Maasakkers[8], Daniel H. Cusworth[9], Riley M. Duren[9], Steven S. Brown[6], Carsten Warneke[6], Colm Sweeney[7], Phillip Stratton[4,10], Alan Brewer[6], Sunil Baidar[5,6], Ezra J. T. Levin[11,12]

[1]Institute for Data, Systems, and Society, Massachusetts Institute of Technology, [2]Department of Aeronautics and Astronautics, Massachusetts Institute of Technology, [3]NOAA/NESDIS, [4]NOAA Air Resources Laboratory, [5]Cooperative Institute for Research in Environmental Sciences (CIRES), University of Colorado Boulder, [6]NOAA Chemical Sciences Laboratory, [7]NOAA Global Monitoring Laboratory, [8]SRON Space Research Organisation Netherlands, [9]Carbon Mapper, Inc, [10]Department of Atmospheric and Oceanic Science / Cooperative Institute for Satellite Earth System Studies (CISESS), University of Maryland, [11]Energy Institute, Colorado State University, [12]Department of Systems Engineering, Colorado State University.

*Tai-Long He, Daniel J. Varon
Email: tlhe@mit.edu, dvaron@mit.edu

This PDF file includes:

- Supporting text
- Figures S1 to S15
- Tables S1
- Legends for Movie S1
- SI References

Other supporting materials for this manuscript include the following:

- Movie S1

Supporting Information Text

Introduction.

This Supporting Information includes seven text sections, fifteen figures, one table, and one movie.

Text S1 describes the preparation work for the VLMR experiment.
Text S2 describes the lookup-table method used for the GOES ABI retrievals.
Texts S3-S5 provide quantification and retrieval methods for TROPOMI, VIIRS/SLSTR, and PACE-OCI.
Text S6 contains detailed information about the aircraft and truck-based in situ measurements and mass-balance calculations of source rates.
Text S7 discusses the comparison of GOES ABI scan modes and the sensitivity test on the moving-average window applied to GOES-18 mesoscale imagery and GOES-19 7-second imagery.

Figure S1 shows an example of forecast plume advection from HYSPLIT simulations used in planning the VLMR experiment.
Figure S2 shows the methane retrievals from Sentinel-3A and VIIRS overpasses over the release sites.
Figure S3 illustrates the instrumental spectral response functions associated with methane bands on the LEO satellites.
Figure S4 compares the PACE-OCI methane retrievals using the 1.6 μm and 2.13 μm reference bands.
Figure S5 summarizes the aircraft and the PUMAS mobile measurements around the two release sites and shows the NASA AVIRIS-3 retrieval of the test release prior to the main blowdown.
Figure S6 shows the angular wind direction geometry in the aircraft spiral mass-balance calculation.
Figure S7 shows the methodology for estimating the vertical layer thickness for a given aircraft loop in a given vertical profile.
Figure S8 shows the PUMAS mobile measurements of 3D winds and attenuated aerosol backscatter during the experiment.
Figure S9 shows a schematic of the PUMAS mobile lab driving path and time series of CH4 concentration measurements made from PUMAS.
Figure S10 illustrates the PUMAS mobile lab driving path and methane measurements, broken down into seven individual segments.
Figure S11 shows the saturation test on the Picarro gas analyzer.
Figure S12 compares in situ aircraft profiles with the corresponding GOES-19 ABI plume retrievals corresponding to the first two mass-balance estimates in Figure 3A in the main text.
Figure S13 shows a sensitivity test of GOES ABI IME and source-rate time series to the size of moving average windows.
Figure S14 shows the performance comparison between the five GOES ABI scan modes.
Figure S15 plots the sensitivity test on moving average window size for the GOES-18 mesoscale imagery.

Table S1 summarizes the average error statistics from the sensitivity test on delay time in calibrating aircraft measurements.

Movie S1 shows video footage of the methane plumes derived from GOES ABI.

Text S1: Preparation of the VLMR experiment.

Preparations for the VLMR gas pipeline blowdown experiment involved coordination across multiple NOAA laboratories and collaboration with the gas pipeline operator. Instrument deployment options were evaluated, including aircraft, mobile laboratory, and satellite observations. Site access, road conditions, and expected wind conditions were assessed to

determine whether the mobile sampling platform could reliably intercept the plume. To support planning, HYSPLIT forecast simulations were performed in advance to predict plume transport and dispersion (e.g., Figure S1). HYSPLIT simulations were initiated approximately one week prior to the experiment using long-range weather forecast model results and were updated regularly as new meteorological forecast model results became available.

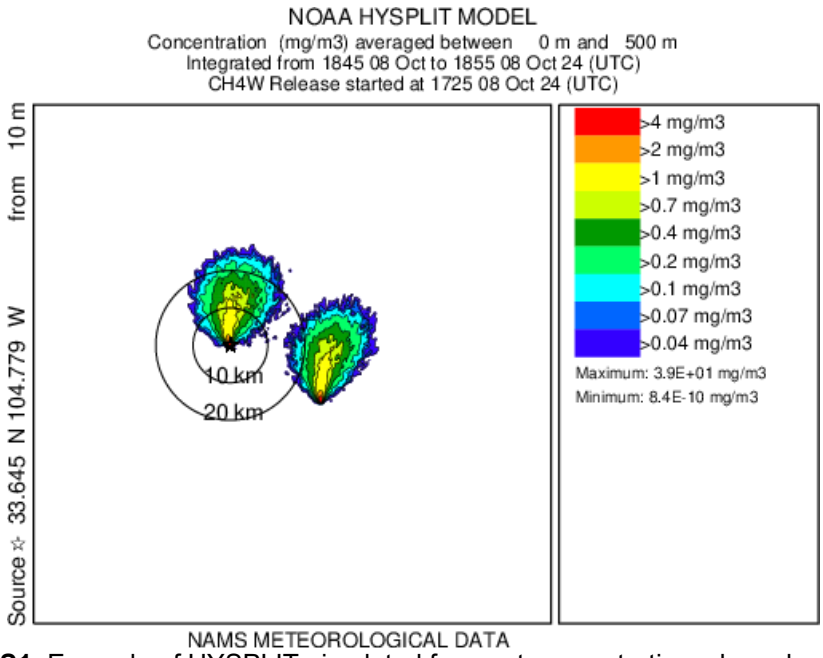

Figure S1. Example of HYSPLIT-simulated forecast concentrations, based on forecast meteorology, used for planning before the event started. This forecast graphic covers a 10-minute period from 1845-1855 UTC, which would occur during the 2nd hour of the actual event. The actual forecast graphic for field use included much more information (lat/longs, roads, etc.). The simplified version shown here does not include geolocation information, due to restrictions on the release of proprietary business information.

Text S2: GOES ABI retrieval and multi-band-multi-pass (MBMP) approach.

We simplify the GOES ABI retrieval algorithm that was originally based on the band-ratio approach of Varon et al. (2021). Rather than performing a full forward radiative transfer calculation for each pixel, we pre-compute a look-up table (LUT) that maps the observed band-averaged radiance ratio between the 1.6 μm and 2.25 μm ABI channels directly to methane column concentrations, and then correct for viewing geometry with a two-way air-mass factor (AMF). We assume a single US-Standard atmosphere, with background CH_4 = 0.66 mol m^{-2} (~1900 ppb), H_2O = 790 mol m^{-2}, and CO_2 = 143.3 mol m^{-2} (~400 ppm). We ignore vertical structure and also neglect CH_4 absorption in the 1.6 μm band (1–2 orders of magnitude weaker than at 2.25 μm).

The LUT is constructed by computing the top-of-atmosphere radiance in the 2.25 μm methane absorption window for a range of methane slant columns (-1 to +10 mol m^{-2}). For each methane slant column, we use molecular absorption cross sections generated from HITRAN line parameters (via the HAPI Voigt line-shape model) for CH_4, H_2O, and CO_2 at the plume elevation (surface elevation + 0.5 km). We then weight the resulting transmittance by the Kurucz solar spectrum (Clough et al., 2005) across the ABI spectral window at 2.25 μm (2220–2270 nm) to compute the band-mean radiance ratio relative to the background (no CH_4 enhancement) case, and store this forward mapping between slant column and band-mean radiance ratio as the LUT. We then invert this relationship via interpolation, so that observed ABI radiance ratios can be

directly mapped to methane slant column enhancement and subsequently converted to vertical column enhancement using the AMF.

For each resulting retrieval image (target), we construct a plume-free reference retrieval image from previous (pre-blowdown) scans and subtract it from the target to isolate methane plumes from surface artifacts. Using the operational 5- and 10-min scan modes, we construct a plume-free reference retrieval image from the average of seven cloud-free scans acquired during the same hour on a previous day when no plume was present, and subtract this reference image from the target retrieval to isolate methane plumes from surface artifacts. For the 30-s and 7-s mesoscale imagery without coverage from previous days, the reference image is instead defined as the mean methane image retrieved from 2 to 1 hours prior to the target scenes. We perform the retrievals and quantify total mass released and emission rate at the native 2-km resolution of the GOES ABI 2.25 μm band.

Text S3: TROPOMI quantification.

An estimate of the Integrated Mass Enhancement (IME) of both plumes at the time of the Sentinel-5P overpass was obtained from the operational TROPOMI CH4 product (Copernicus Sentinel-5P, 2021).

The destriped total column methane data was used. A plume mask was created using a threshold with respect to the median methane concentration of the surrounding pixels (corresponding to a roughly 300km×300km scene with 710 pixels with successful retrievals), where the threshold (1930 ppb) was chosen to visually match the plume extent.

Methane concentrations were converted to enhancements by subtracting a reference concentration, computed as the median of the scene without the plumes. Subsequently, the enhancements were converted to per-pixel masses, using the surface pressure from the CH4 product, the area of the footprint of the pixel, and the column averaging kernel of the methane retrieval.

For the column averaging kernel, the plume was assumed to be fully in the lowest layer of the TROPOMI retrieval (corresponding to the layer up to around 750 m above the surface). The IME was then computed by summing this value for all pixels in the plume. Uncertainties were computed by propagating the standard deviation of the concentration of the background pixels and the uncertainty of the CH4 retrievals within the plumes as independent contributions.

Text S4: VIIRS/SLSTR retrieval and quantification

For VIIRS and SLSTR, methane enhancements were retrieved with a Multi-Band Multi-Pass (MBMP) method, slightly adapted from the one described by de Jong et al., 2025. Two adaptations were made, both improving internal consistency.

First, we used the following formula for the MBMP signal:

$$\Delta R_{MBMP} = \frac{c_{2.2} R_{2.2}}{R_{2.2}{}'} - \frac{c_{1.6} R_{1.6}}{R_{1.6}{}'}$$

where the constants ci are the ratios of the median values of the band radiances on the reference day Ri' and on the measurement day Ri for the band with wavelength i μm. We then performed radiative transfer simulation to estimate methane concentration fields using ΔRMBMP.

Second, an additional median subtraction was performed. The MBMP method yields methane enhancements with respect to an arbitrary reference concentration. To more accurately compute the enhancement in the plume, after finding the plume masks, the median of the pixels in the scene outside the plume masks was subtracted before computing the IME.

Otherwise, the same methods as in de Jong et al. (2025) were used, including destriping and resampling to a 500m-resolution grid of roughly 100 km × 100 km. The plume mask was also found using the same methods, by normalizing the enhancements with respect to the uncertainty and selecting areas with a deviation of more than 1.5 standard deviation and selecting only the two largest such areas per overpass. The uncertainty was similarly computed by summing the per-pixel uncertainties.

Figure S2 shows the resulting methane retrievals from Sentinel-3A and VIIRS over the western and eastern release locations on 8 October 2024. The 20:45 UTC NOAA-21 overpass is not included in Figure 2 in the main text because it falls outside the period of interest.

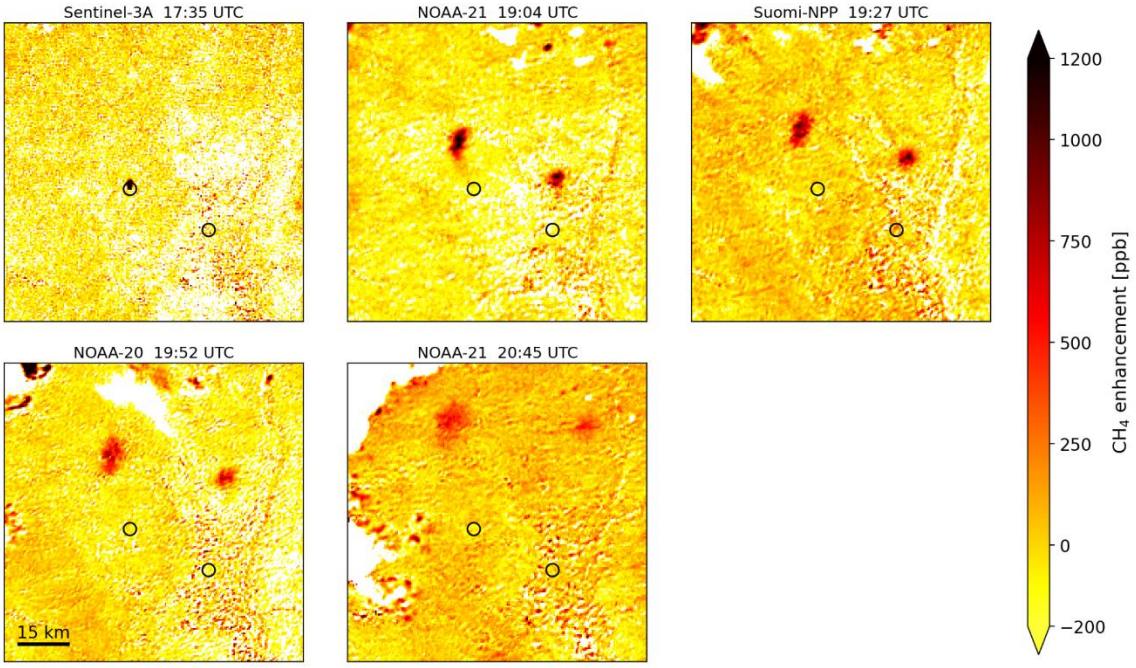

Figure S2. VIIRS and Sentinel-3A methane enhancement retrievals over the two VLMR release locations (black circles) on 8 October, 2024. White regions indicate retrievals masked by clouds. Retrieved total plume masses (sum of both plumes) are 104±26, 348±114, 352±109, 313±101, and 335±125 t, in chronological order.

Text S5: PACE-OCI retrieval

Methane enhancement retrievals were also performed using the Ocean Color Instrument (OCI) aboard the Plankton, Aerosol, Cloud, ocean Ecosystem (PACE) satellite, which launched on the 8th of February 2024. OCI has a nominal resolution of 1.2 km and has three SWIR bands relevant for methane retrievals, centered at 1.615, 2.130 and 2.260 μm respectively, as shown in Figure S3. The same retrieval method described in Text S4 was used, but using bands at 2.1 and 2.3 μm. Data was resampled to the same 500m-resolution grid used for the VIIRS retrievals.

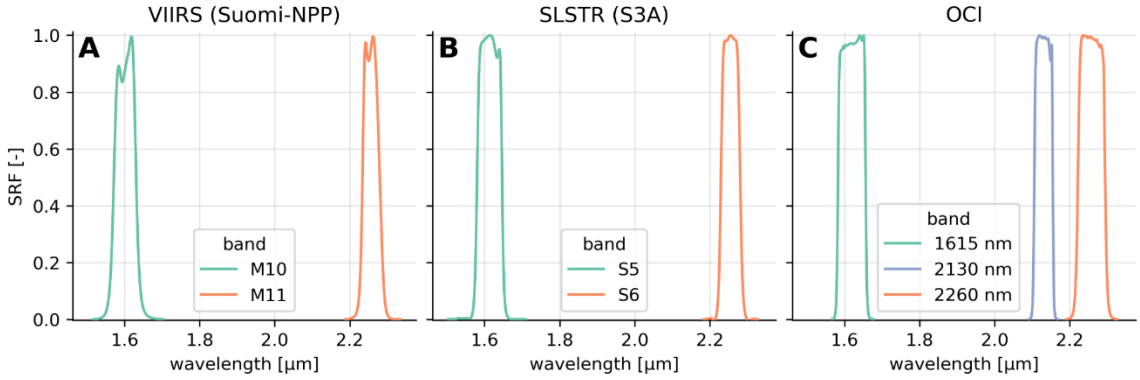

Figure S3. Instrument Spectral Response Functions (SRFs) of bands relevant to methane retrieval for (A) VIIRS on Suomi-NPP, (B) SLSTR on S3A and (C) OCI on PACE. SRFs for OCI were sourced from Meister et al. (2024).

As the 2.2 μm band is much closer to the μm 2.3 band compared to the usual 1.6 μm reference band used for other instruments, this combination is less sensitive to artifacts such as caused by differences in relative albedo of the surface, as illustrated in Figure S4. This smaller difference results in a cleaner retrieval. The OCI data was subsequently processed using the approach used for the VIIRS/SLSTR data as described in Text S5.

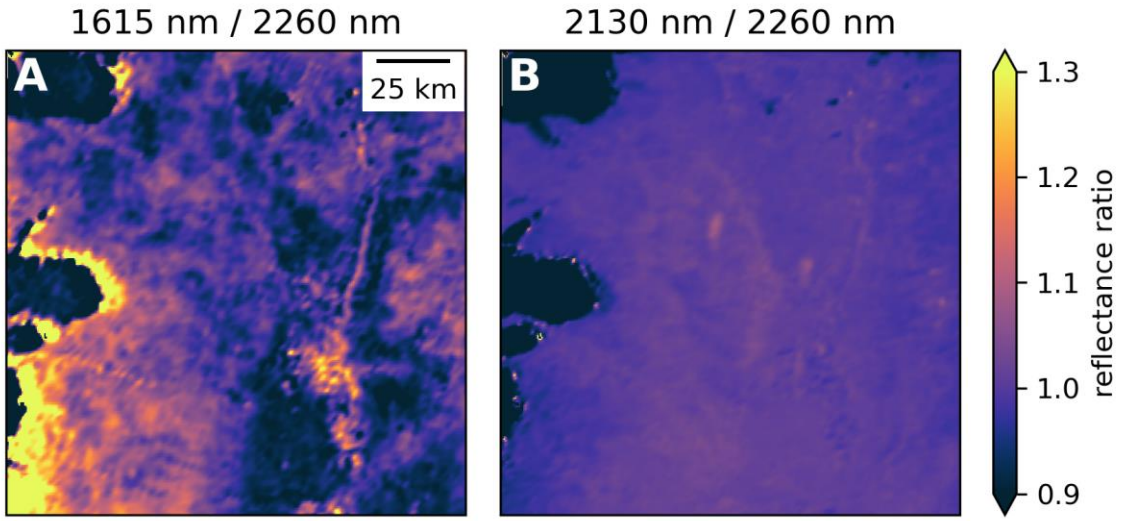

Figure S4. Ratios of reflectance measured in different SWIR bands of PACE-OCI for the overpass of the VLMR event. Comparing the usual 1.6 μm reference band (Standard Gain (SG) one used on PACE-OCI) and the 2.13 μm band to the 2.26 μm band, which has the strongest methane absorption. Shown are (A) 1615 nm SG over 2260 nm and (B) 2130 nm over 2260 nm.

Text S6: In situ measurements and mass-balance calculation

As shown in Figure S5, the NOAA/ChampionX Mooney aircraft entered the experimental region at 16:20 UTC and initially flew to the western release site, where it remained in a holding pattern before the blowdown began. After the western release began at 17:22 UTC, the aircraft performed two near-source spiral profiles around the western source from 17:29 to 17:52 UTC, with loop altitudes of approximately 100–600 m agl. The maximum methane mixing ratio measured by the aircraft was 226 ppm at 17:45 UTC during western-source sampling. The aircraft then sampled the eastern source with two spiral profiles from 18:06 to 18:28 UTC at approximately 130–355 m agl. After completing the eastern profiles, the aircraft returned to the western plume for additional in-plume spirals to characterize plume vertical structure and boundary-layer depth, followed by two cross-plume transects at 375 and 510 m agl approximately 25 km downwind of the western source. Mass-balance estimates of source rate from these transects (not shown in Fig. 3) are similar to the earliest spiral-based estimate (~200 t h-1), but with much more uncertain timing because of the long travel distance. Aircraft measurements concluded at approximately 19:45 UTC.

The NOAA PUMAS mobile laboratory sampled the eastern plume downwind of the release site. The truck measured a peak 1-s-average methane mixing ratio of 289 ppm at 17:46 UTC, approximately 1.85 km downwind of the eastern source and about 10 min after the blowdown began. It then moved to approximately 8.45 km downwind of the eastern source and conducted three crosswind transects. The first transect, from 18:20:29 to 18:33:31 UTC, measured a peak 1-min-average methane enhancement of 63 ppm but did not cover the full

plume width and was therefore not used for the emission-rate estimate. The following two transects, from 18:35:30 to 18:45:29 UTC and from 19:08:30 to 19:19:31 UTC, measured peak 1-min-average methane enhancements of 10.1 ppm and 0.4 ppm, respectively. These two transects captured the full plume width and were used to estimate eastern-source emission rates by mass balance.

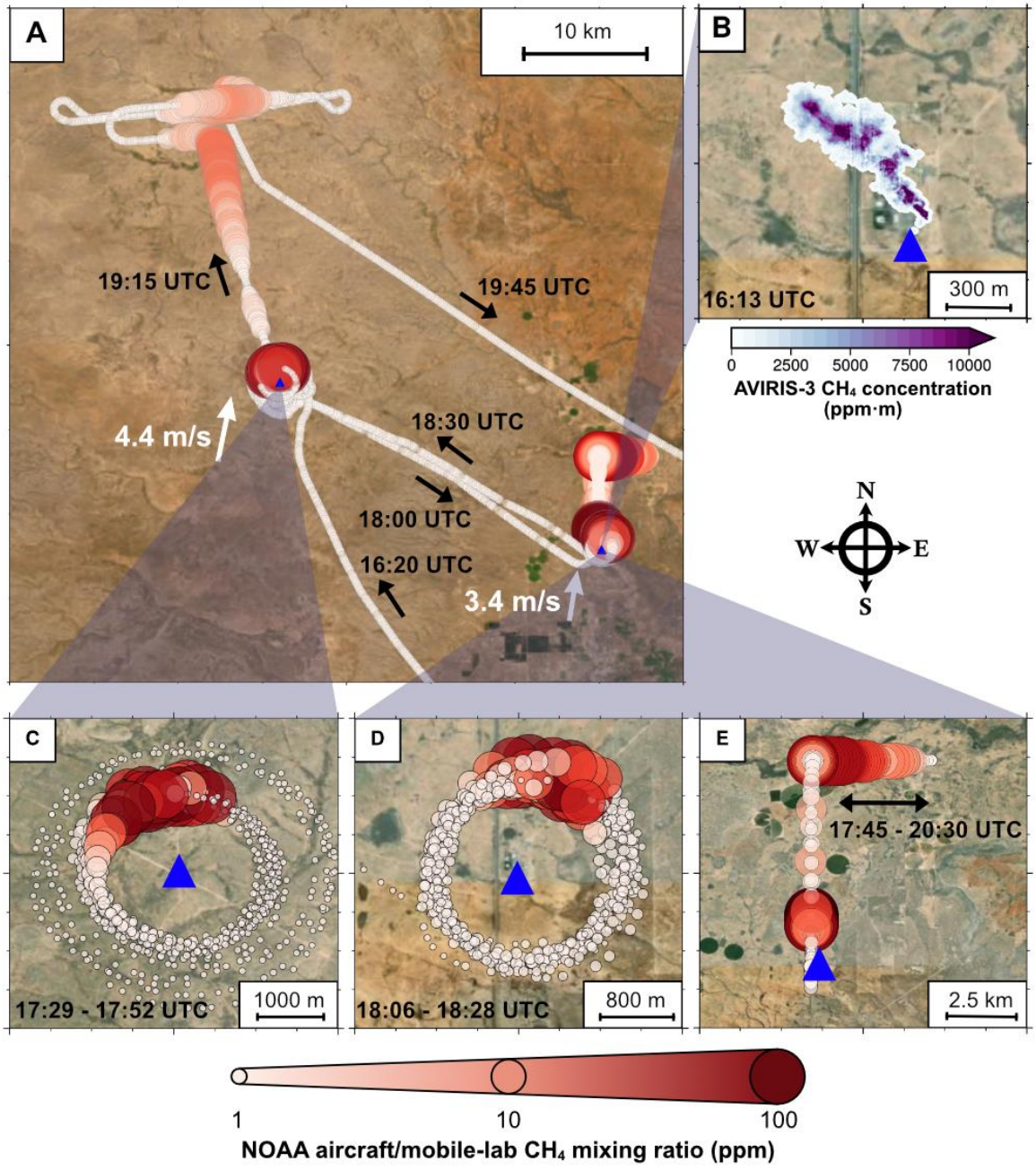

Figure S5. Aircraft and ground-based methane measurements during the VLMR experiment. (A) Methane mixing ratios (ppm) from the NOAA/ChampionX Mooney aircraft and PUMAS mobile laboratory. (B) AVIRIS-3 detection of the pre-blowdown test release. (C–D) Mooney spirals around the western (C) and eastern (D) release sites. (E) PUMAS plume transects near the eastern site. Blue triangle symbols mark the pipeline blowdown locations. Black arrows indicate direction of the Mooney aircraft and PUMAS mobile lab.

Text S6.1: Aircraft mass-balance analysis

Four wind treatments were used to estimate uncertainty in the aircraft mass-balance source rates for each loop of the NOAA Mooney spiral profiles:

Aircraft winds, loop mean: wind speed and direction from loop-mean 1-Hz aircraft GPS-based winds reported by Aspen Avionics.
Aircraft wind speed with plume-inferred direction: loop-mean aircraft wind speed combined with a concentration-weighted source-to-aircraft direction, representing the wind direction required to transport the plume from the source to the observed location.
HRRR winds: wind speed and direction from the NOAA HYSPLIT HRRR archive, interpolated to the source location and sampling time.
NAM winds: wind speed and direction from the NOAA HYSPLIT NAM archive, interpolated to the source location and sampling time.

HRRR is archived at 3-km horizontal resolution using hourly forecast cycles, whereas NAM is archived at 12-km resolution using 6-hourly forecast cycles.
The mass-balance methodology considers a cylindrical control surface around the emissions site. To estimate the mass flow rate through this cylindrical surface for a given loop, we sum the mass flow rate through the surface for each second during the loop, factoring in the estimated vertical thickness h of the layer that the loop is assumed to represent. For a given loop, the summation goes from the start time of the loop (0) to the end time of the loop (T):

$$\sum_0^T [C(t) - C_b(t)] \cdot \Delta w(t) \cdot \Delta h \cdot U_p(t) \cdot \beta(t) \quad \text{(Eq. S2)}$$

where

C(t) (μmol CH4 / mol air) = the second-by-second concentration of CH4 measured during the loop by the Mooney aircraft;
Cb(t) (μmol CH4 / mol air) = the estimated background concentration of CH4 during the loop;
Δw(t) (m) = the second-by-second distance that the aircraft travelled during the loop;
Δh(m) = the estimated vertical thickness of the vertical layer associated with the loop;
Up(t) (m s-1) = the second-by-second component of the horizontal wind velocity perpendicular to the direction of the aircraft at the location of the aircraft concentration measurement during that second (see Figure S4 below);
β(t) [g m-3 / (μmol CH4 / mol air)] = the second-by-second factor to convert from the volume/volume concentration measurements to mass/volume concentration values.

Since the control surface is a cylinder, we have used the orientation of the sampling site relative to the emissions source rather than the aircraft's heading relative to the ground, although the difference between the two is generally very small. It should be noted that the distance from the source varied during each loop, i.e., the cylinder's cross-section was not a circle. For each one-second measurement, the horizontal distance traveled was calculated as the radial distance for that measurement multiplied by the change in angle relative to the source location during that measurement.

Further, it should be noted that the elevation of each loop was not constant. For each loop, a concentration-weighted average elevation was used. This methodology ensures that the loop elevation used in the overall mass balance calculation reflects the measurements with strongly elevated CH4 concentrations.

The mass flow rate for a given loop is then related to the time-resolved emissions rate from the source by subtracting an estimate of the travel-time from the source to the loop.

More details regarding the methodology are described below.

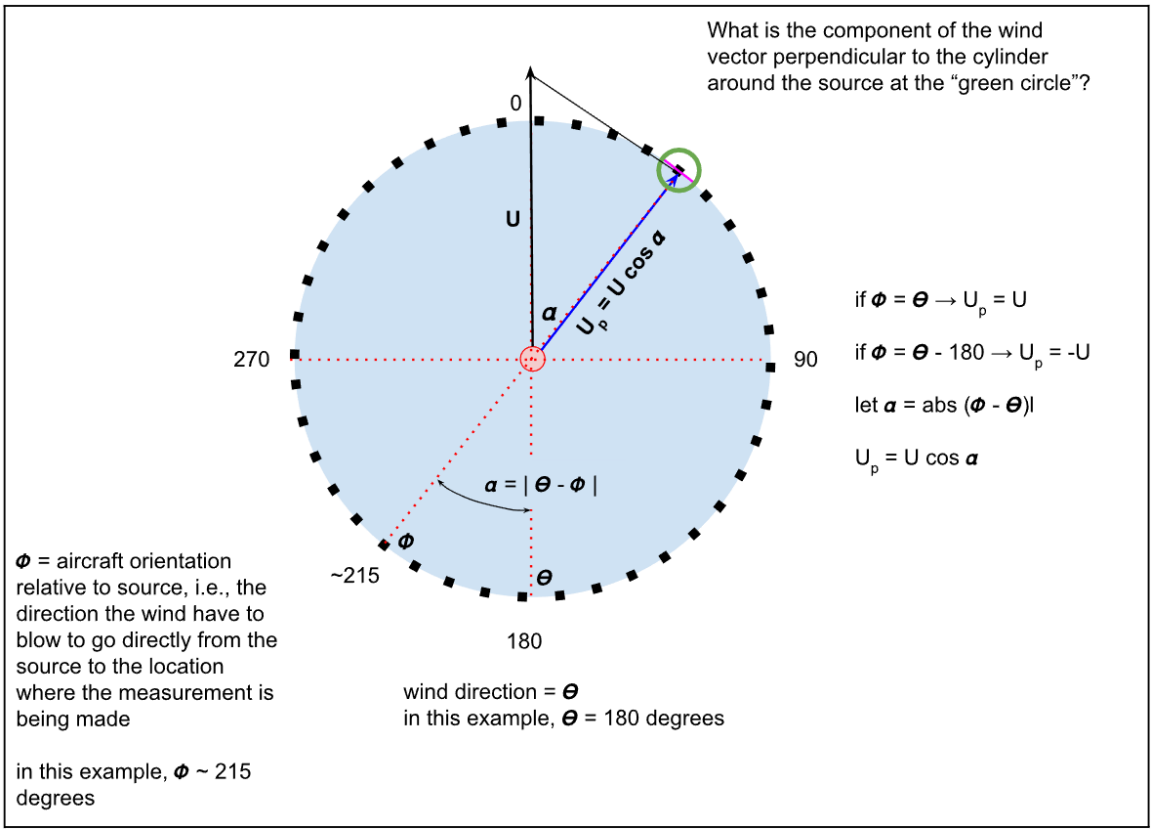

Figure S6. Angular wind direction factor in mass balance calculation.

Loop by Loop Analysis

Distinct loops were defined around the eastern and western source locations, in which the aircraft distance from the source was less than 2 km throughout the loop. The start of each East loop was assumed to be at an aircraft orientation relative to the source of ~58 degrees (the aircraft was approximately West-Southwest of the site). At that location, the wind direction would have had to be ~58 degrees for the wind to blow directly from the source location to the aircraft location. The start of each West loop was assumed to occur at a comparably defined orientation of ~325 degrees when the aircraft was Southeast of the West emissions site. This value ensured that the enhanced methane concentrations measured, at roughly 180 degrees, were well separated from the start and end of each loop. Also, the first loop around the West emissions site started at about 325 degrees.

The vertical layer thickness represented by a given loop in a given profile is assumed to be the difference in elevation from the midpoint between the loop and the next lowest-elevation loop and the midpoint between the loop and the next highest elevation loop in that profile. For the lowest elevation loop in a profile, the layer is assumed to extend to the surface. For the highest elevation loop, the layer is assumed to extend the same vertical distance above the loop as the difference in the loop elevation between the loop and the midpoint between the loop and the next lowest-elevation loop. This aspect of the methodology is shown schematically in Figure S7 below.

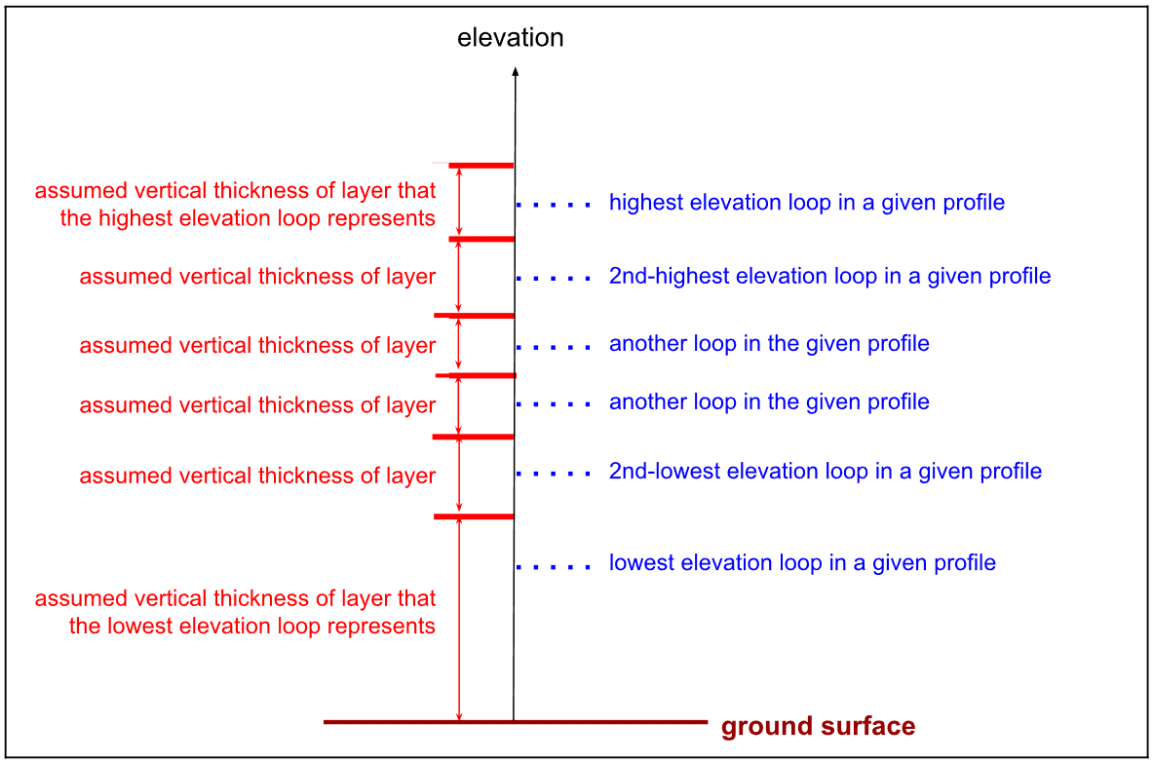

Figure S7. Vertical layer thickness estimation for a given loop in a given profile.

The aircraft GPS-associated measurements (lat, long, u, v, altitude, etc.) were delayed approximately 4-7 seconds due to data-processing and transfer constraints. The physical and chemical measurements (P, T, RH, CH4-ppbv, etc.) were delayed approximately 11 seconds primarily due to the inlet length. In the merged dataset from the aircraft flights, the physical and chemical measurements are automatically adjusted for the 11-second inlet-related delay. To match the GPS data to the physical-chemical measurement data, a specified number of seconds must be subtracted from each GPS timestamp's "UTC-Start" (seconds).

Numerical sensitivity experiments were conducted for GPS delays of 4, 5, 6, and 7 seconds to calibrate aircraft wind direction measurements. A statistical summary for the entire series of numerical experiments is shown below in Table S1. Based on these results, a GPS time lag of ~6 seconds was used as the "base" value in this analysis. However, the emissions rates estimated with time lags of 4-7 seconds are relatively consistent, and the sensitivity to this assumption is not large.

Table S1. Average error, absolute error, and RMSE of wind direction as a function of delay time.

Delays (s)	Ave error (deg)	Ave abs error (deg)	RMSE (deg)	Ave error (deg)	Ave abs error (deg)	RMSE (deg)
0	-23.9	23.9	90.8	-23.0	23.7	167.5
4	-10.3	10.4	45.3	-7.7	12.1	102.1
5	-7.0	8.0	35.7	-3.9	11.1	94.0
6	-3.6	6.8	28.2	-0.1	11.6	91.6
7	-0.2	6.0	24.7	3.6	12.1	94.7

Each loop took on the order of ~80 seconds to complete, and during each loop, CH4 enhancements were measured at 15-20 seconds during the loops. The CH4 background for each aircraft loop was estimated as the 40th percentile of concentration values in that loop. Using other non-enhanced percentile values to characterize the non-enhanced "background concentrations"

made only a trivial difference in the mass- balance emissions estimates and is not considered an important uncertainty in the mass- balance calculations.

The emission time for a given source differs from the aircraft measurement time because it takes time for the plume to travel from the source to the concentration measurement location. To estimate the uncertainty range in the travel time, we have estimated the minimum emissions time for a given profile by subtracting the maximum loop travel times (distance from source divided by the minimum loop wind speed (from methods 1, 2, 3, and 4)) from the time of the first loop in a given profile. The maximum emissions time for a given profile was estimated by subtracting the minimum loop travel times (distance from source divided by the maximum loop wind speed, from methods 1, 2, 3, and 4) from the time of the last loop in a given profile. The range in possible emissions times estimated in this way is used to estimate the uncertainty in the emissions time for any given profile.

Text S6.2: Mass balance analysis using NOAA PUMAS Mobile Lab

The PUMAS Doppler lidar operates at 1.54 μm, a wavelength at which atmospheric backscatter is dominated by aerosols rather than molecular scattering; signal-to-noise ratio therefore depends strongly on aerosol loading. The combined dynamics and aerosol information enables a robust boundary layer height retrieval based on mixing (e.g., w variance), wind shear, and aerosol gradient (Tucker et al., 2009). Figure S8 shows the wind and aerosol measurements from this experiment. The range resolution of both lidar channels was 62 m and the temporal resolution was 15 seconds for each profile of horizontal winds (i.e., one conical scan) and 1 second for the vertical wind channel. The wind speed shows a very consistent and well-defined low-level jet in the morning before sunrise, which decays as the daytime well-mixed boundary layer starts to grow. Boundary layer winds strengthened gradually from morning to midday. The boundary layer height grew substantially over the study period (17:36 - 19:00 UTC), making this measurement essential for accurate retrievals of methane emissions.

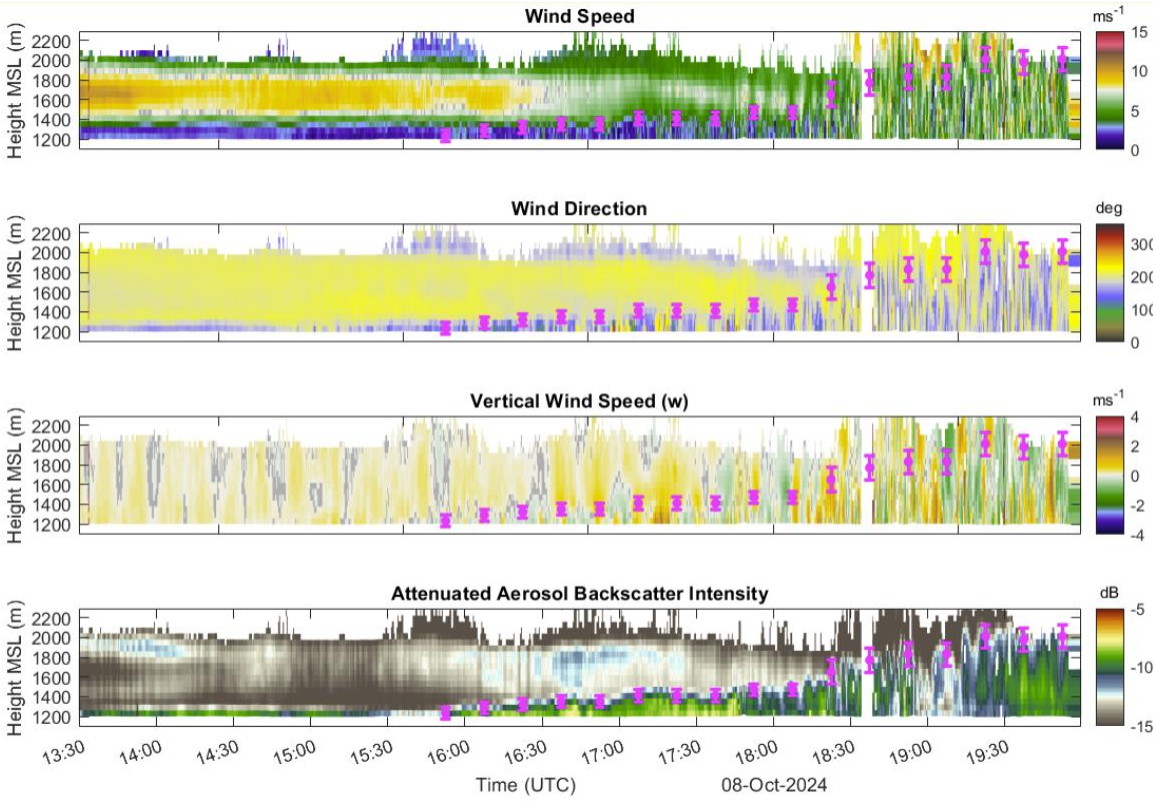

Figure S8. PUMAS lidar profile time series of (a) wind speed, (b) wind direction, © vertical wind, and (d) attenuated backscatter during the experiment. The pink points are boundary layer heights with uncertainty bars.

An Aeris instrument was deployed on PUMAS to measure methane and ethane at 1 Hz. The analyzer is a high-precision trace gas instrument based on mid-infrared (mid-IR) laser absorption spectroscopy for continuous, real-time measurements of methane and ethane (C2H6). By targeting fundamental vibrational absorption features in the mid-IR spectral region, the analyzer achieves high selectivity and sensitivity with low cross-interference from other atmospheric gases. The instrument offers sub-ppb detection limits, rapid response time (1 s), and stable operation suitable for both laboratory and field deployments. Its applications include urban air quality monitoring, natural gas leak detection, and characterization of methane sources, with ethane serving as a tracer to help distinguish fossil fuel emissions from biogenic methane. The analyzer was calibrated before and after the pipeline blowdown experiment. An online zeroing system was incorporated to zero the analyzer using ultra-zero air to track instrument drift during operation.

As shown in Figure S9, the PUMAS truck was near the eastern release site at the time of release, then, given the approximately southerly wind direction, PUMAS drove north with the goal of executing cross-plume transects far enough downwind that the methane would be well-mixed within the boundary layer. The first large plume intercept while driving north was incidental and did not transect the entire plume width, so it is not suitable for a representative emissions estimate. The later east-west legs are useful for emissions estimates, as the data shows that all or at least more than half of the plume was transected each time. The distance between the eastern release site and the east-west transects is ~8.5 km, which corresponds to ~28–35 minutes of transport time, given average winds of 4-5 m s-1 measured in the PBL. This is enough time for two eddy turnovers, and the observed plume widths are approximately three times the mixing height. Both are good indicators of the vertically well-mixed assumption.

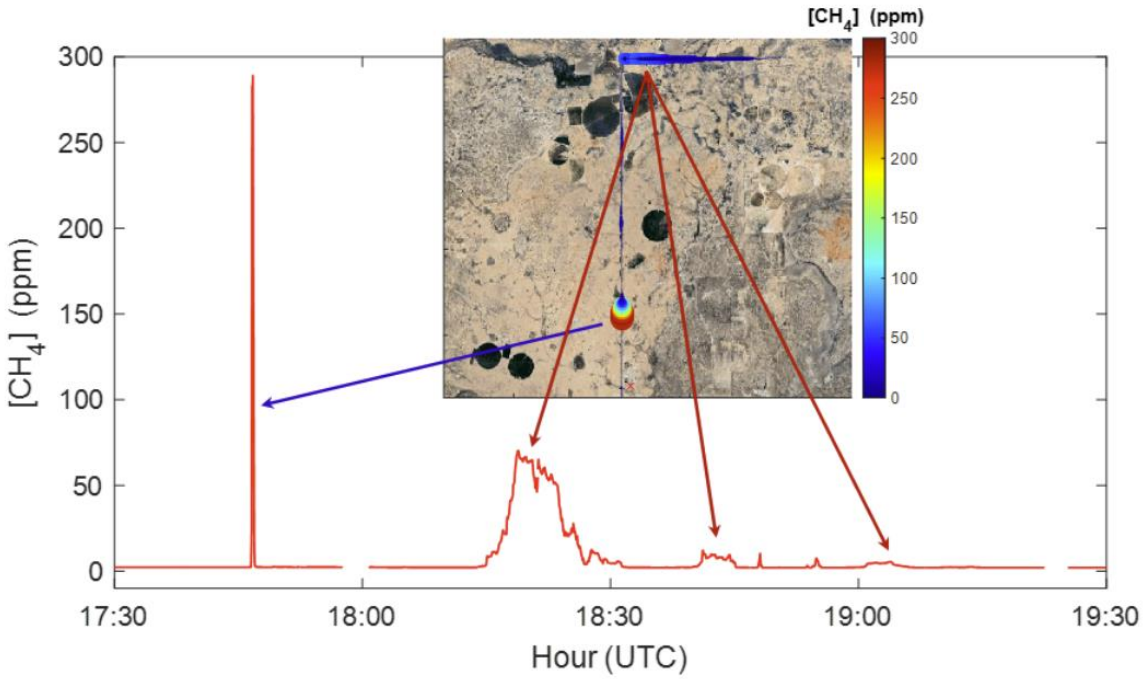

Figure S9. Time series of methane measured downwind of the eastern release facility during the pipeline blowdown experiment on Oct 8, 2024. The embedded map indicates the observation locations where methane enhancements were detected.

To apply mass-balance analysis to PUMAS measurements, we consider a plane (curtain) downwind of the emissions site and calculate the mass flow rate through this plane. We do this by summing the mass flow rate through the plane for each second during a given transect. In the following equation, for a given transect, each term is a function of time, and the summation goes from the start time of the transect (0) to the end time of the transect (T).

$$\sum_0^T [C(t) - C_b(t)] \cdot \Delta w(t) \cdot \Delta h \cdot U_p(t) \cdot \beta(y) \quad \text{(Eq. S3)}$$

where

C(t) (μmol CH4 / mol air) = the second-by-second concentration of CH4 measured during the transect;

Cb(t) (μmol CH4 / mol air) = the second-by-second background concentration of CH4 during the transect;

Δw(t) (m) = the second-by-second distance that the mobile lab travelled during the transect;

Δh(m) = the second-by-second height of the plume at the location of the concentration measurement location during that second;

Up(t) (m s-1) = the second-by-second component of the horizontal wind velocity perpendicular to the direction of the mobile lab at the location of the concentration measurement during that second;

β(t) [g m-3 / (μmol CH4 / mol air)] = the second-by-second factor to convert from the volume/volume-based concentration measurements to mass/volume concentration values.

The mass flow rate for a given transect is then related to the emissions rate from the source by subtracting an estimate of the travel-time from the source to the transect, i.e., to account for the fact that the measurements occurred after the plume had traveled for some time downwind of the source.

We carried out an extensive series of numerical experiments and sensitivity analyses with respect to how the terms in Eq. S2 were calculated, and on the basis of this analysis, we estimate the overall uncertainty in the mass-balance flux estimates for each mobile transect to be ±25%.

As shown in Figure S10, the mobile-lab transects occurred along the east-west road about 9 km downwind of the source. The mobile lab driving path can be divided into 7 sections. The methane fluxes were calculated using Eq. S3, with h(t) set as the lidar-determined mixing height. We fit a seventh-order polynomial to h(t) in Figure S7 to time-interpolate a time-varying h across each transect. To get the boundary-layer averaged wind Up in Eq. S3, we vertically-average the wind profiles between ground and mixing height h(t), time-average nearby profiles (using a low-pass filter) to remove turbulent noise, then curve-fit to match their time-evolution with the 1 Hz methane measurements.

To estimate the travel time associated with truck-measured methane enhancements, we integrated the PUMAS wind backwards in time from the measurement time average, and determined when the integral reached the distance between the concentration-weighted transect location and the release point. This methodology may lead to an underestimate of the travel time because the plume likely did not follow a perfectly straight line from the source to the transect. This analysis gives an estimated travel time of ~30 minutes for the first transect from 18:20–18:30 UTC (red squares in Fig. S10), and ~26.5 minutes for the second transect from 18:35–18:45 UTC (green circles in Fig. S10).

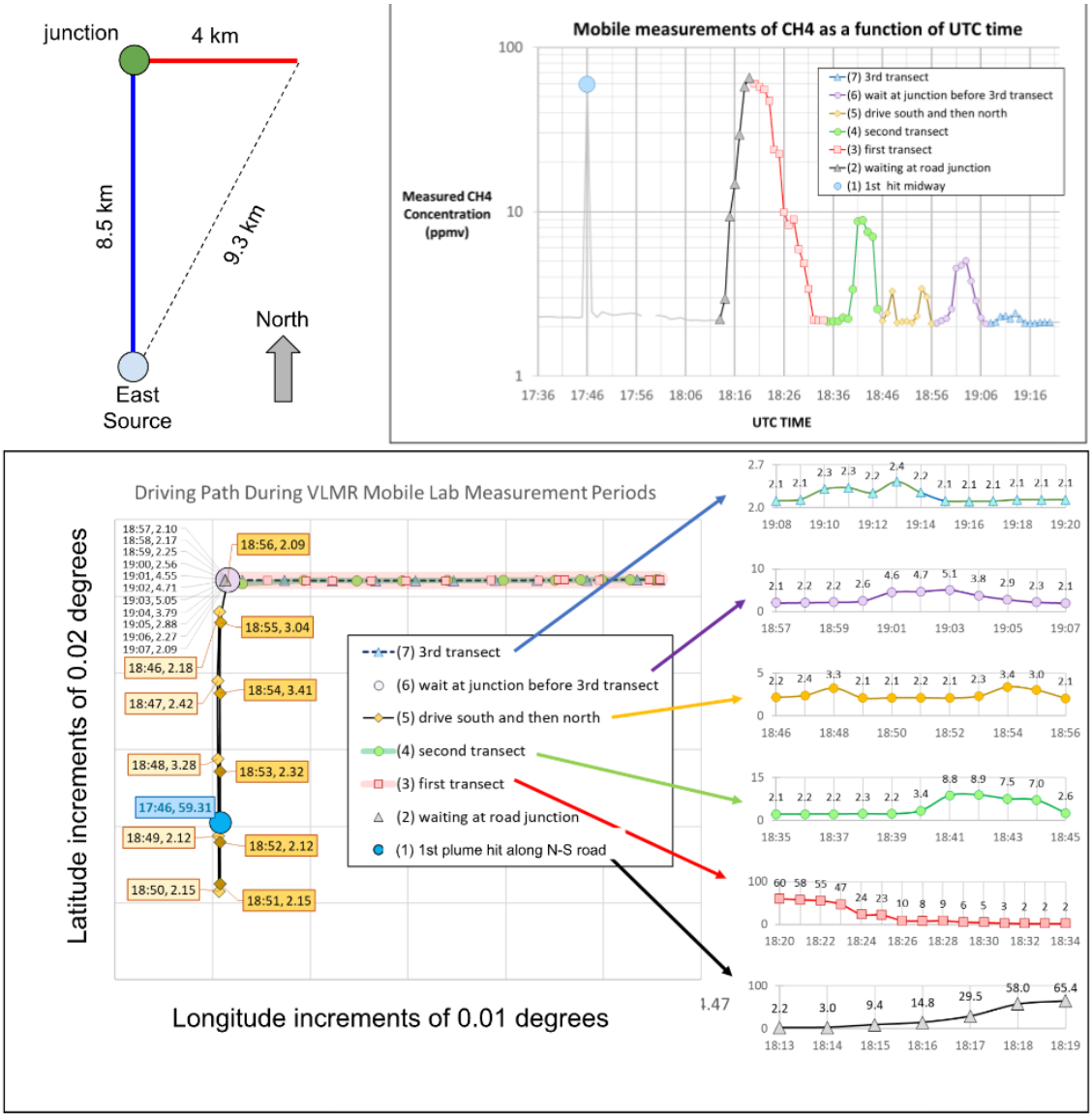

Figure S10. (Top) Schematic of the PUMAS mobile lab driving path and time series of CH4 concentration measurements made from the mobile lab. (Bottom) Seven segments of the mobile lab driving path and associated CH4 measurements.

Text S6.3: Diagnosing underestimated in situ mass-balance source rates

NOAA's Global Monitoring Laboratory installed a Picarro G2401-m aboard a ChampionX (formerly Scientific Aviation) Mooney aircraft for the National Observations of Greenhouse Gases using Aircraft Profiles (NOGAP) campaign beginning in mid-October 2024. The inlet was located in the wing, and approximately 2 m long, ~3 mm (⅛") O.D. stainless steel tubing with a flow rate of 255 sccm. Methane (CH4), carbon dioxide, carbon monoxide, and water vapor were reported every 2.5 seconds and interpolated to a 1 Hz time base. Additionally, ChampionX provided GPS and wind data calculated similar to Conley et al. (2017). The trace gas data time base has been shifted approximately 16 seconds for inlet and data transfer time lags to best align with the aircraft measurements. The Picarro instrument was calibrated immediately before and after the NOGAP campaign and run against a standard tank before and after each flight to determine instrument drift. We estimate uncertainties of ±2 ppb CH4 relative to the WMO X2004A scale, and ±0.2 m s-1 for wind speed.

The Picarro G2401-m manual states the analyzer is linear up to 20 ppm CH4. To test the linearity of measurement above this threshold, the analyzer used during the October 8, 2024 flight was calibrated in the laboratory using a standard of 193.38 (±0.18) ppm CH4 in air. As shown in Fig. S11, the analyzer retrieved a value of 208.1 (± 1.2) ppm CH4. The highest value sampled on the October 8 flight was 225 ppm, and 25 plumes peaked above 49 ppm. We estimate an additional uncertainty of 2–8% for measurements between 49 and 225 ppm CH4. We further note that when making these CH4 measurements well outside the intended range of the instrument, the Picarro processing software takes approximately 8–10 seconds to report a value of this magnitude. This is significantly longer than the approximately 2–2.5 seconds between measurements when sampling background air. This delay in the measurement occurred both in the laboratory experiment and during the October 8 flight when the aircraft sampled the highest plume concentrations.

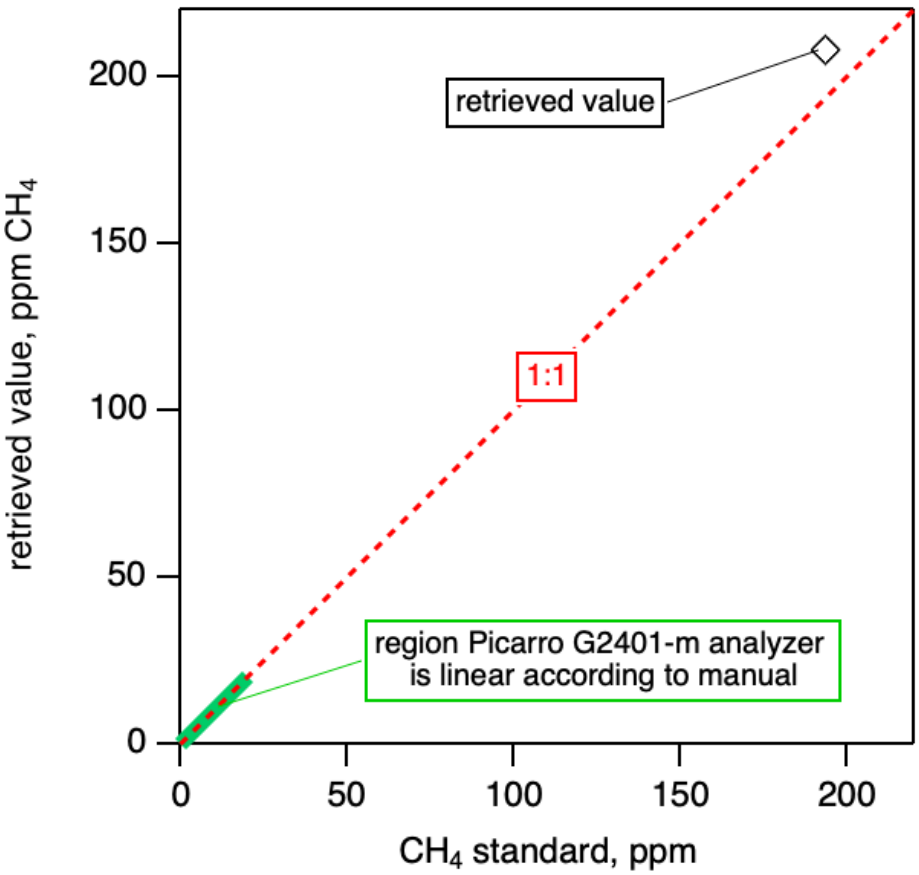

Figure S11. Laboratory results from the Picarro G2401-m analyzer sampling from a nominal 193 ppm CH4 in air standard. The region the manual states the analyzer has a linear response is highlighted in green.

Figure S12 provides a more detailed illustration of how this concentration-dependent measurement delay could contribute to an underestimation of the flux rates derived from in situ measurements. Figure S12A and B show the wind-rotated aircraft profiles over the western source, overlaid with the closest GOES-19 ABI 7-s methane retrievals, corresponding to the first two mass-balance estimates in Figure 3A. Several features could contribute to the underestimation of source rates from mass-balance analysis using the in situ measurements. First, the releases are highly transient, so no steady-state plume develops for in situ sampling.

Second, the longer measurement time at elevated methane concentrations reduces the effective sampling frequency within high-concentration plume cores.

Figures S12C and D further demonstrate the crosswind cross-sections of aircraft measurements around the western source for the two aircraft spiral profiles. The two sampling profiles showed substantial spatial heterogeneity, with the highest methane enhancement represented by only a small number of measurements. This pattern is consistent with the longer measurement time of the Picarro analyzer at concentration levels outside its nominal measurement range, which reduced the effective sampling density within the plume core.

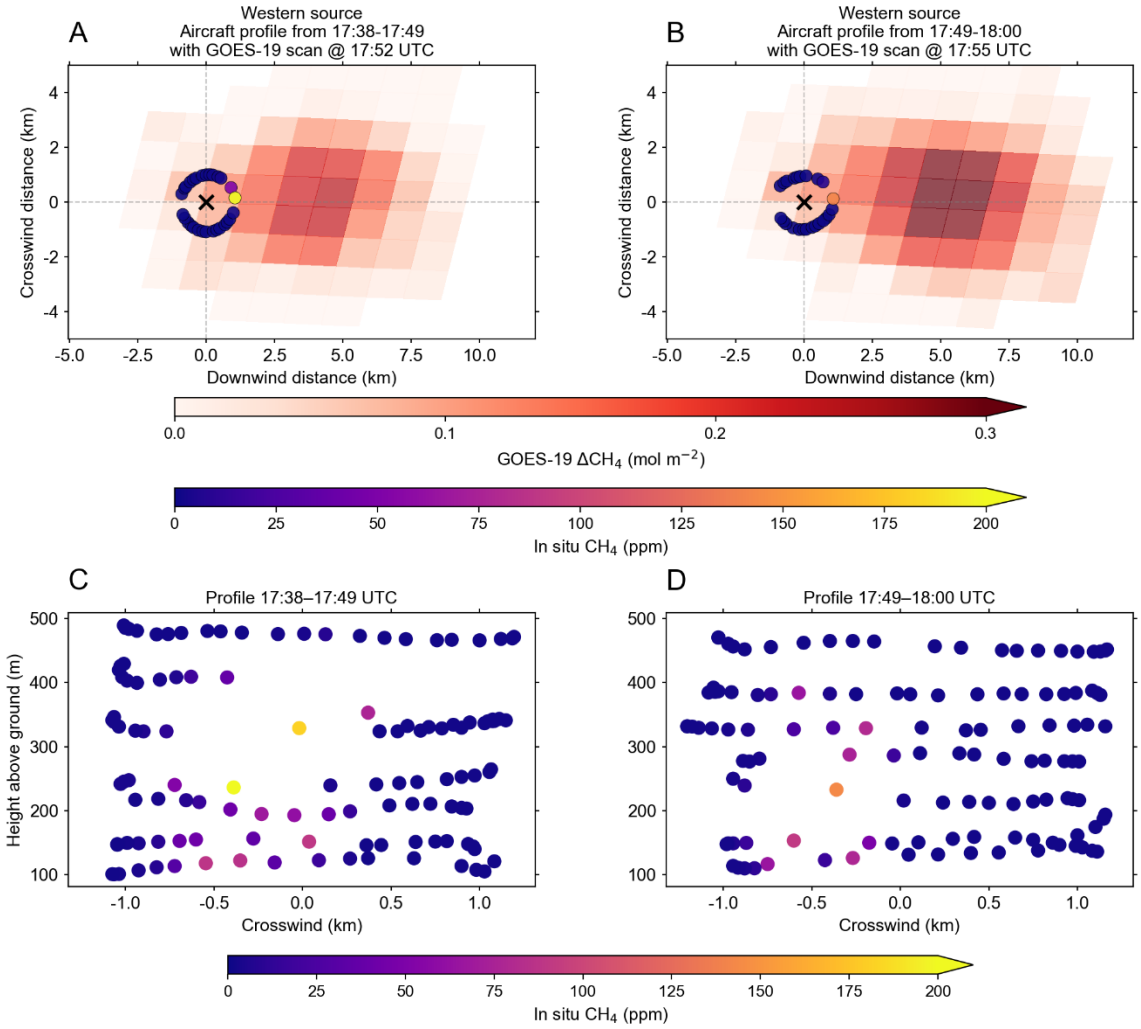

Figure S12. (A, B) Wind-rotated in situ measurements and corresponding GOES-19 ABI plume retrievals for the first two mass-balance estimates in Figure 3A. In situ measurements are shown as colored scatter points and GOES-19 ABI 7-second methane retrievals are shown as shaded fields. (C, D) Crosswind vertical cross-sections of aircraft measurements around the western source corresponding to the two spiral profiles.

Text S7: Comparison between GOES ABI scan modes and sensitivity test on moving averaging

Figure S13 shows the time series of IME and source rates from the raw retrievals and from moving averages calculated using 5-, 9-, and 15-min windows. The choice of averaging window

has little effect on the IME results. For the western source-rate estimates, the differences among the averaging windows are also small, with differences of approximately 10% occurring only near the peak source rates. The eastern source-rate estimates are more sensitive to the averaging window: the 15-min moving average produces a substantially lower peak source rate, whereas the 5-min moving averages are calculated from only three data points and are therefore less statistically robust. Overall, the 9-min moving-average window preserves the main temporal features of the source-rate time series without introducing apparent artifacts, and the ±1σ range provides a reasonable representation of the uncertainty associated with retrieval variability.

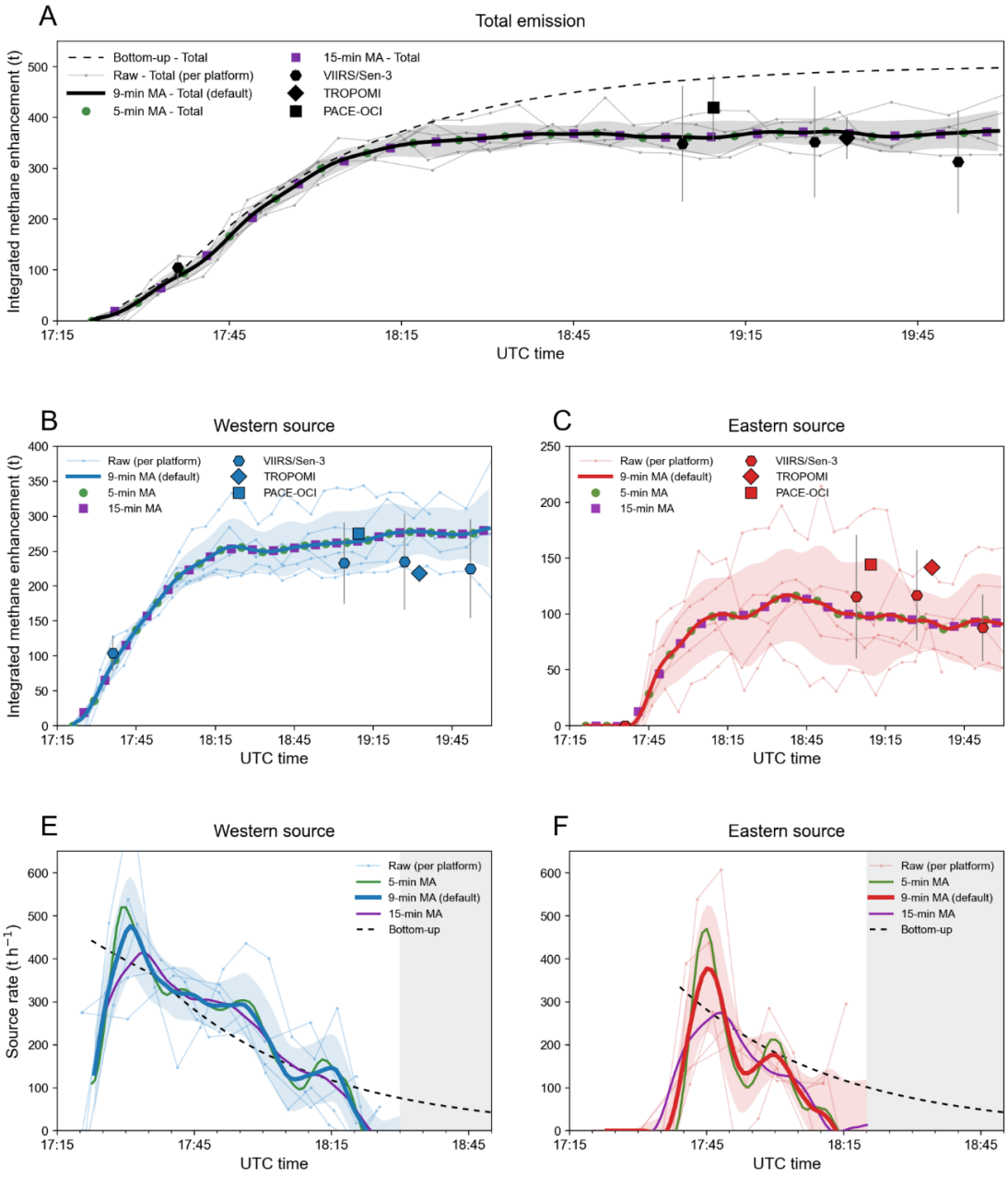

Figure S13. Sensitivity test of GOES ABI IME and source-rate time series to the size of moving average windows. (A-C) Time series of IME for total emissions, western source, and eastern

source. Thin lines show the raw retrievals from each data stream; solid lines show the 9-min moving averages used in the main text; green circles show the 5-min moving averages; and purple squares show the 15-min moving averages. The markers with errorbars represent IME derived from LEO satellites. (E,F) Time series of source-rate estimates. Thin lines show the raw retrievals from each data stream; solid lines show the 9-min moving averages used in the main text; green lines show the 5-min moving averages; and purple lines show the 15-min moving averages. Dashed lines indicate the bottom-up model estimates.

Figure S14 compares the performance of different GOES ABI scan modes by calculating the signal-to-noise ratio (SNR) and the root mean square error (RMSE) for each scan. The SNR is defined as follows:

$$SNR = 10 \times \log_{10} \frac{P_{signal}}{P_{noise}} \quad \text{(Eq. S4)}$$

where P_{signal} is the average power of the isolated plume signal with non-plume pixels replaced by zeros and P_{noise} is the average power of background pixels (masking out plumes, water body, and clouds). Here we define the powers of imagery as

$$P_{signal} = \sum_{i,\ in\ plume} x_i \text{ and } P_{noise} = \sum_{i,\ in\ background} x_i \quad \text{(Eq. S5)}$$

A higher SNR indicates a stronger ability to isolate plume signals from the background, while a lower RMSE reflects greater precision in methane retrieval. The GOES-18 mesoscale imagery shows the best performance in both isolating plume signals and retrieving methane with high precision. The GOES-19 7-second imagery performs comparably to the GOES-18 and GOES-16 full-disk imagery, whereas the GOES-16 CONUS scans exhibit lower SNR and higher RMSE.

The smoothed GOES-18 mesoscale retrievals outperform all operational scan modes, increasing the SNR from -13 and -10 to values above -18 and reducing the RMSE by 50%, from 0.08 mol m-2 to below 0.04 mol m-2. We also performed a sensitivity test on the choice of window size for smoothing the GOES-18 mesoscale retrievals. As shown in Figure S15, we find that both SNR and RMSE improve as the GOES-18 mesoscale imagery is averaged from 1-min to 2-min, and further to 5-min and 10-min windows. The best performance is achieved with 5-min and 10-min windows, which yield nearly identical results. For consistency, we adopt the 5-min window in the main text.

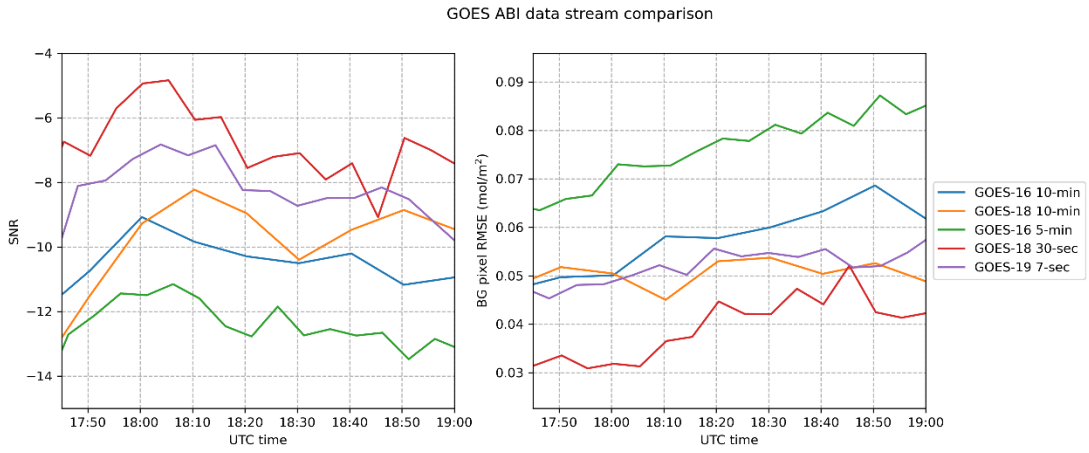

Figure S14. Time series of signal-to-noise ratio (SNR) and background pixel root mean square error (RMSE) for five GOES ABI data streams during the experiment.

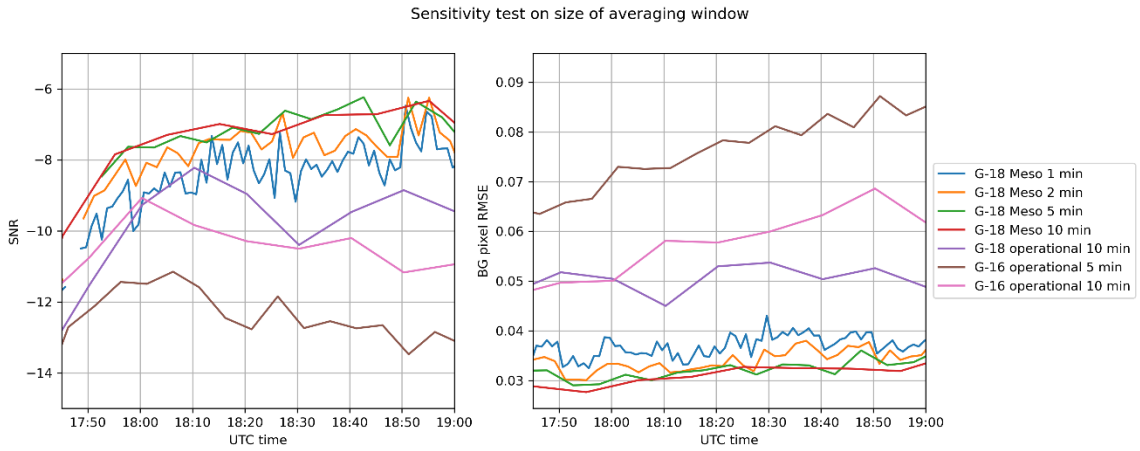

Figure S15. Time series of SNR and background pixel RMSE for GOES-18 mesoscale imagery smoothed using different window sizes, compared with operational GOES ABI data streams.

Movie S1 (separate file). Video footage of the methane plumes observed by GOES ABI.

SI References

1. Varon, D. J., Jervis, D., McKeever, J., Spence, I., Gains, D., and Jacob, D. J.: High-frequency monitoring of anomalous methane point sources with multispectral Sentinel-2 satellite observations, Atmos. Meas. Tech., 14, 2771–2785, https://doi.org/10.5194/amt-14-2771-2021, 2021.
2. Clough, M.W. Shephard, E.J. Mlawer, J.S. Delamere, M.J. Iacono, K. Cady-Pereira, S. Boukabara, P.D. Brown, Atmospheric radiative transfer modeling: a summary of the AER codes, Journal of Quantitative Spectroscopy and Radiative Transfer, Volume 91, Issue 2, 2005, Pages 233-244, ISSN 0022-4073, https://doi.org/10.1016/j.jqsrt.2004.05.058.
3. de Jong, T. A., Maasakkers, J. D., Irakulis-Loitxate, I., Randles, C. A., Tol, P., & Aben, I. (2025). Daily global methane super-emitter detection and source identification with sub-daily tracking. Geophysical Research Letters, 52, e2024GL111824. https://doi.org/10.1029/2024GL111824
4. Gerhard Meister, Joseph J. Knuble, Julia A. Barsi, Robert Bousquet, Leland H. Chemerys, Robert E. Eplee, Ulrik Gliese, Samuel Kitchen-McKinley, Shihyan Lee, Jeffrey W. McIntire, Frederick S. Patt, P. Jeremy Werdell, "On-orbit OCI characterization measurements from the first six months of the PACE mission," Proc. SPIE 13192, Sensors, Systems, and Next-Generation Satellites XXVIII, 131920A (20 November 2024); https://doi.org/10.1117/12.3033581
5. Tucker, S. C., C. J. Senff, A. M. Weickmann, W. A. Brewer, R. M. Banta, S. P. Sandberg, D. C. Law, and R. M. Hardesty, 2009: Doppler Lidar Estimation of Mixing Height Using Turbulence, Shear, and Aerosol Profiles. J. Atmos. Oceanic Technol., 26, 673–688, https://doi.org/10.1175/2008JTECHA1157.1.
6. Conley, S., Faloona, I., Mehrotra, S., Suard, M., Lenschow, D. H., Sweeney, C., Herndon, S., Schwietzke, S., Pétron, G., Pifer, J., Kort, E. A., and Schnell, R.: Application of Gauss's theorem to quantify localized surface emissions from airborne measurements of wind and trace gases, Atmos. Meas. Tech., 10, 3345–3358, https://doi.org/10.5194/amt-10-3345-2017, 2017.